Faculty of Physics und Astronomy
Ruprecht-Karls-University Heidelberg

Bachelor Thesis

in Physics

submitted by

Jonathan Friedrich Herbrich

born in Tübingen

march 2025

Mechanical strain field driving Landau-Zener transitions in the borosilicate glass BS 3.3

This Bachelor theis was conducted by Jonathan Friedrich Herbrich
at the Kirchhoff-Institute for Physics
under the supervision of
Prof. Dr. C. Enss

Landau-Zener Dynamik im Borosilikatglas BS 3.3 induziert durch ein mechanisches Verzerrungsfeld

Die Eigenschaften amorpher Festkörper bei niedrigen Temperaturen unterscheiden sich von denen von Kristallen aufgrund von atomaren Tunnelsystemen (TS). Diese TS sind verantwortlich für niederenergetische Anregungen in amorphen Festkörpern. Das Standard Tunnel Modell (STM) beschreibt diese Eigenschaften phänomenologisch. Das STM beschreibt TS als zwei Niveau Systeme mit einer homogen verteilten Energieaufspaltung und Asymetrieenergie.
In dieser Arbeit werden die dielektrischen Eigenschaften der Probe BS 3.3, einem amorphen Festkörper, untersucht. Dies geschieht indem wir unsere Probe einem elektrischen Feld aussätzen, während wir die Energieaufspaltung mit einem mechanischem Verzerrungsfeld modifizieren. Ein mikrostrukturierter LC-Resonator, welcher auf unsere Probe gesputtered wird, wurde für diese Messungen benutzt. Das mechanische Verzerrungsfeld wird durch Biegung der Probe mit einem piezoelektrischen Aktuator (PEA) erzeugt und koppelt an die TS aufgrund deren deformations Potentials. Wir zeigen dass die für ein elektrisches Vorspannungsfeld entwickelte Landau-Zener Theorie mit einem mechanischen Zerrungsfeld gemessene Daten beschreiben kann.

The properties of amorphous solids at low temperatures deviate in comparison to their crystalline counterparts because of low energy excitations, occurring due to atomic Tunneling Systems (TSs). The Standard Tunneling Model (STM) allows for a phenomenological description of these properties. The STM expresses the TSs at sufficiently low temperatures as two level systems with a flatly distributed energy splitting.
In this thesis, the dielectric rf-response of BS 3.3 glass is studied by probing the sample with an electric field while varying the energy splitting by applying a mechanical strain field. A microfabricated superconducting LC-resonator, sputtered on the sample, was used for these measurements. The strain field is applied by bending the sample with a piezoelectric actuator and couples the TSs to the field via the deformation potential. We show that a framework based on Landau-Zener transitions, originally developed for the description of electrically biasing, can also describe our mechanical biasing measurements.

Contents

1. Introduction

Crystals are solids with a periodic structure. At low temperatures, their thermal properties can be predicted by the Debye model [Deb12]. It assumes only acoustic phonons with long wavelengths are present. In contrast to crystals, the structure of amorphous solids only has a short range, but no long range order and their bond lengths and angles are statistically distributed. Due to the long phonon wavelengths present at low temperatures, this should not affect the thermal properties and the Debye model would again be sufficient to predict the thermal properties. Experiments performed by Zeller and Pohl [Zel71] have shown that this is not the case and that at low temperatures the specific heat capacity and thermal conductivity deviate from the expected values. It was concluded that in contrast to crystals, additional low-energy excitations have to take place in amorphous solids.

Thus, Anderson *et al* [And72] and Phillips [Phi72] developed the standard tunneling model (STM) independently as a way to describe these excitations. The model assumes that, at low temperatures, a single atom or a group of atoms can have two energetically similar equilibrium positions. They are separated by a potential barrier and the available thermal energy at low temperatures is not sufficient to overcome it, and changes are only possible because of the quantum mechanical tunneling effect. While small changes were made to the model, for example in the distribution function of the tunneling systems [Dou80, Ens89], it remained solid in the prediction of later experimental findings. Examples are acoustic [Cla94, Cla00], dielectric [Rog97, Fro77] and ultrasonic absorption [Hun77, Hun72] measurements.

Amorphous solids in the form of amorphous oxide layers are used in microfabricated quantum circuits. However they were found to be a source of noise [Bur14] and decoherence [Ku05] and are thus a recent subject of investigations. In recent experiments, the dielectric rf-response of an amorphous sample, while slowly varying an electric bias field, was investigated, showing that the bias field can increase the dielectric loss [Fre21] by inducing Landau-Zener dynamics. A microfabricated superconducting LC-resonator was used for these measurements.

In this thesis, we want to repeat this phenomena, using the glass BS 3.3 as our sample, but instead of electric bias fields, we slowly vary an acoustic bias field by bending the sample, thus inducing a mechanical strain field. For this purpose a piezoelectric actuator is used. The actuator already touches the sample and thus bends the sample if its extended. As a result, parameters of our tunneling systems are modified, as these couple to the strain field via deformation potential.

This thesis is split into five parts. In chapter 2 we introduce the underlying theoretical framework to understand the results of our measurements. We start by establishing the dielectric function, which can be split into a real and an imaginary part and will be the main indicator to measure the rf-response of our sample. Following this, we explore the properties of amorphous solids at low temperatures and introduce the standard tunneling model. We will use the model to explain how our sample couples to applied electric fields and how the dielectric function responds to such fields. In the last step we expand this by introducing Landau-Zener transitions taking place while an additional bias field is applied. In chapter 3 we take a look at the measurement principle. We will show how our sample is set up inside the cryostat and how the RF-signal reaches the resonator. We then explain how to extract the real part and loss of the dielectric function out of the resonance curves of our resonator. We close this chapter by presenting how the piezoelectric actuator works and how it induces a strain field within our sample. The fourth chapter focuses on the results of our measurements. We start with equilibrium measurements with no strain field applied followed by non-equilibrium measurements. There we will take a look if expansion and contraction or an increased preload on the sample change the dielectric response. Then we compare the dielectric function during biasing for different input powers. The last chapter summarizes our findings and provides an outlook on future measurements.

2. Theory

In this chapter we introduce the theoretical background behind the measurements we carried out. We start of by introducing the dielectric function of amorphous solids. This is followed by a discussion of the properties of glass, introducing the standard tunneling model, discussing the dynamics of the glass with an applied electric field and changing temperature. In the end we discuss how this response changes if we induce a strain field.

2.1 Dielectric Function

If an electric field $\vec{F}$ is applied and a dielectric material is placed within it, the field acts upon the dielectric and local charges are redistributed. This leads to the formation of electric dipoles or already existing dipoles are rotated in accordance to the electric field. The sum of those smaller dipoles adds up to form the macroscopic polarization $\vec{P}$ proportional to the electric field

$$\vec{P} = \varepsilon_0 \chi \vec{F} \tag{2.1}$$

with the dielectric constant ε_0 and the dielectric susceptibility χ. Inserting $\vec{P}$ into the definition of the displacement field $\vec{D}$ results in

$$\vec{D} = \varepsilon_0 \vec{F} + \vec{P} = \varepsilon_0 (1 + \chi) \vec{F} = \varepsilon_0 \varepsilon \vec{F} \quad , \tag{2.2}$$

were we defined the dielectric function as $\varepsilon = 1 + \chi$. It measures the ability of our material to store energy. If an alternating electric field is applied the polarization follows with a delay adding an imaginary part to our equation

$$\varepsilon(\omega) = \varepsilon'(\omega) + \mathrm{i}\varepsilon''(\omega) \tag{2.3}$$

and is mainly frequency dependent. The real part ε' contains the processes that are in phase with the driving field and thus gives us information about the energy stored in the dielectric, while the imaginary part ε'' contains dissipation processes that are out of phase with the driving field. One of the main measurement variable we will use in the description of dielectric materials is the dielectric loss tangent

$$\tan(\delta) = \frac{\varepsilon''}{\varepsilon'} \tag{2.4}$$

with the loss angle δ. It is used to describe energy that is lost because of dissipation and will in the following be called loss.

2.2 Low Temperature Properties of Amorphous Solids

We will use glass, an amorphous solid, as our dielectric medium for our experiments. Here only a brief discussion of the difference between amorphous solids and crystal solids will be presented, a more detailed discussion can be found in [Ens05]. Cooling down a melt can result in two different outcomes. Typically if one cools it slowly, the result is a crystal with a periodic structure. Rapid cooling however results in an amorphous solid, with a short range, but no long range order. This changes the properties of the solid, resulting in a different thermal conductivity κ and specific heat capacity C_V. For crystals the Debye model predicts that both are proportional to T^3 in the low temperature limit. For amorphous solids this deviates to a near linear temperature dependency $C_\mathrm{V} \propto T^{1.3}$ for the heat capacity [Zel71] and quadratic temperature dependency for thermal conductivity. This leads to the assumption that additional low-energy excitations take place at low temperatures.

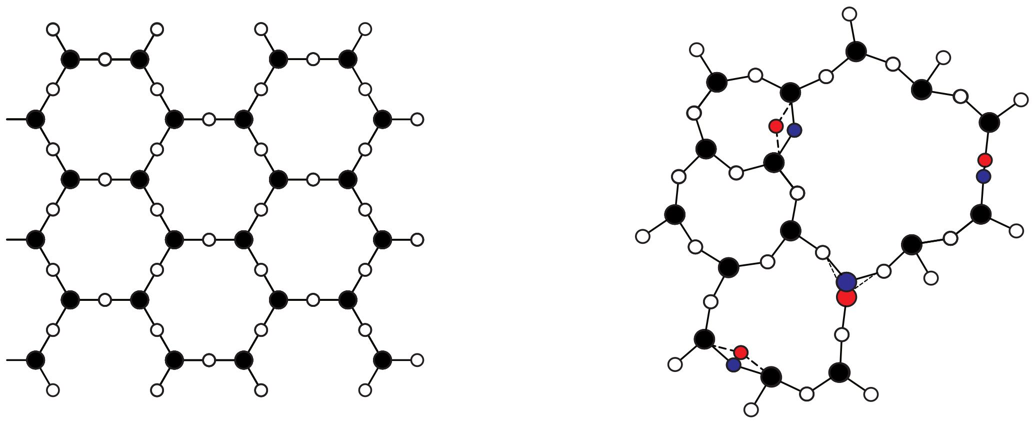

Figure 2.1: Representation of a cross section of a crystalline (left) and an amorphous (right) SiO_2 solid. The contorted structure of the amorphous solid allows for multiple energetically stable equilibrium positions of a single atom or a group of atoms. For the sake of clarity adapted from [Zac32, Hun74].

Due to the lack of a regular lattice in amorphous solids atoms or groups of atoms can have more than one energetically favored position, as can be seen in Figure 2.1 (marked by red and blue colored atoms). On a microscopic level a stable position is described with the harmonic oscillator as a well potential, with particles of mass m having a ground state energy $\hbar\Omega/2$ above the low point of the well. The potential barrier is defined by the barrier height V which the particle has to overcome

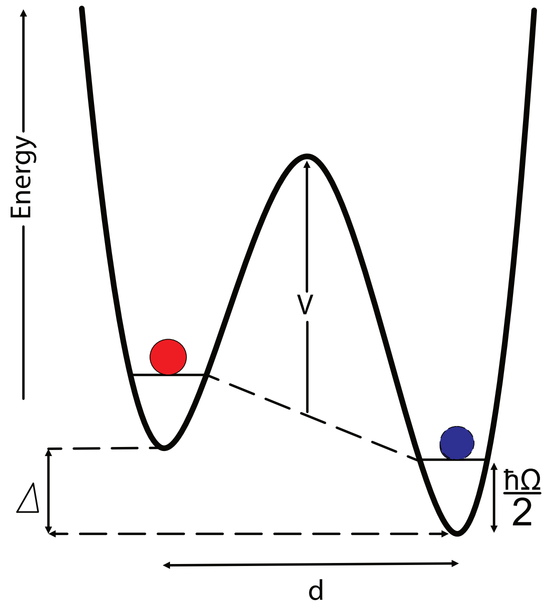

Figure 2.2: Illustration of the two equilibrium positions of a single particle represented by the double well. The wells are separated with the distance d, the potential barrier of height V and difference in asymmetry energy Δ. The particle of mass m has a ground state energy $\frac{\hbar\Omega}{2}$ above the low point of each well. Adapted from [Phi81].

to change positions, the asymmetry energy Δ describes the difference between the minima of the equilibrium states and d is the distance between the wells. At low temperatures $T < 1\,\mathrm{K}$ TLS can reside in the ground state or the first excited state with a difference in energy E, fully introduced in Equation 2.21, called energy splitting. The population difference ΔN is given by [Ens05]

$$\Delta N = N \tanh\left(\frac{E}{2k_\mathrm{B}T}\right) \tag{2.5}$$

with N the number of systems and the latter term describing the probability of a single system residing in the ground state. This shows that the state a systems reside in is directly linked to the available thermal energy $k_\mathrm{B}T$ and at low temperatures $k_\mathrm{B}T \ll E$ most systems are in the ground state, but a phonon with energy equal to the energy splitting of a particular system can be absorbed raising it to the excited state. If we externally introduce more phonons to our sample, we increase the intensity J and thus raise more systems in the excited state. If a phonon hits a system that is already in the excited state a phonon is emitted from the tunneling system lowering its energy to the ground state again. If the intensity is high enough ΔN approaches zero with the result that the number of phonons absorbed and emitted is equal and our system is saturated. This can be quantified with the loss introduced in Equation 2.4

$$\tan(\delta) = \frac{\tan(\delta_0)}{\sqrt{1 + \frac{J}{J_c}}} \tag{2.6}$$

with J_c the critical intensity, describing the moment at which saturation starts to begin [Hun76]. We use the plateau observed for low intensity to define $\tan(\delta_0)$, which normalizes our function. At this stage every phonon can be resonantly absorbed and it increases with lower temperature. If instead of phonons, photons are introduced by an electric field, further called driving field with the field strength F_{ac}, the equation changes to

$$\tan(\delta) = \frac{\tan(\delta_0)}{\sqrt{1 + \frac{F_{ac}}{F_c}}} \tag{2.7}$$

while the underlying process remains the same.

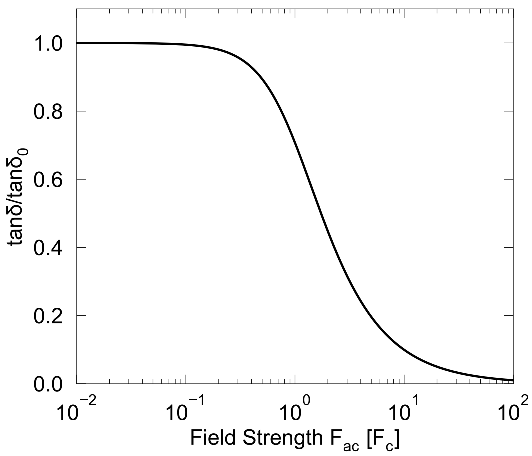

Figure 2.3: Dielectric loss curve, due to resonant interactions with the driving field, dependent on the field strength F_{ac}. At small field strengths the loss has a plateau until it reaches the critical field strength F_c and saturation starts to set in and the loss starts to decrease. At high field strengths the population difference approaches zero and the loss follows accordingly.

2.3 Standard Tunneling Model

The standard tunneling model (STM) was independently developed by Anderson [And72] and Philip [Phi72] to describe the low temperature behavior of amorphous solids and assumes that an atom or groups of atoms can have two equilibrium positions at low temperatures, which we already introduced in Section 2.2 and is best described with a double well potential with a similar low point energy. Now we want to introduce a mathematical framework for the STM.

2.3.1 Two-Level-System

To obtain the energy level of the ground state and excited state for two level systems one can use the time independent Schrödinger equation, resulting in the energy eigenstates E of our double well potential

$$\mathcal{H}\Psi = E\Psi \quad . \tag{2.8}$$

Linearly combining the wave function of two uncoupled single well harmonic oscillators gives us the total wave function

$$\Psi = \alpha\psi_\mathrm{a} + \beta\psi_\mathrm{b} \quad . \tag{2.9}$$

For solving the Schrödinger equation 2.8 with this ansatz from Equation 2.9 the approach as described in [Ens05] is used. Here only the important results are mentioned. Inserting Equation 2.9 into 2.8 results in the energy eigenvalue

$$E = \frac{\langle\Psi|\,\mathcal{H}\,|\Psi\rangle}{\langle\Psi|\Psi\rangle} = \frac{\alpha^2\mathcal{H}_\mathrm{aa} + \beta^2\mathcal{H}_\mathrm{bb} + 2\alpha\beta\mathcal{H}_\mathrm{ab}}{\alpha^2 + \beta^2 + 2\alpha\beta S} \quad . \tag{2.10}$$

Where we introduced the following equations as abbreviations:

$$\mathcal{H}_\mathrm{aa} = \langle\Psi_\mathrm{aa}|\,\mathcal{H}\,|\Psi_\mathrm{aa}\rangle = \frac{\hbar\Omega + \Delta}{2} \tag{2.11}$$

$$\mathcal{H}_\mathrm{bb} = \langle\Psi_\mathrm{bb}|\,\mathcal{H}\,|\Psi_\mathrm{bb}\rangle = \frac{\hbar\Omega - \Delta}{2} \tag{2.12}$$

with $\mathcal{H}_\mathrm{aa/bb}$ the energy expectation values for a single well, where we set the zero point of energy between the minima of the two wells

$$\mathcal{H}_\mathrm{ab} = \langle\Psi_\mathrm{aa}|\,\mathcal{H}\,|\Psi_\mathrm{bb}\rangle = -\frac{\Delta_0}{2} \tag{2.13}$$

$$S = \langle\Psi_\mathrm{a}|\Psi_\mathrm{b}\rangle \quad . \tag{2.14}$$

The interaction energy between the wells is given by $\mathcal{H}_\mathrm{ab}$. S is the overlap of the uncoupled wave functions. We also introduced the tunneling splitting Δ_0 and we can use the WBK[1] approximation to get

$$\mathit{\Delta}_0 = \hbar\Omega e^{-\lambda} \tag{2.15}$$

with λ being the tunneling parameter that is dependent of the particle mass, barrier height and distance between wells

$$\lambda = \frac{d}{2\hbar}\sqrt{2mV} \quad . \tag{2.16}$$

Since we only look at the properties of amorphous solids at low temperatures, we only need the two lowest eigenstates. We can calculate them by minimizing the energy of the two single harmonic oscillators

$$\frac{\partial E}{\partial a} = 0 \quad \text{and} \quad \frac{\partial E}{\partial b} = 0 \tag{2.17}$$

[1] Gregor Wentzel, Hendrik Anthony Kramers, and Léon Brillouin, 1926

leading us to the equation

$$0 = (\mathcal{H}_{\mathrm{aa}} - E)(\mathcal{H}_{\mathrm{bb}} - E) - (\mathcal{H}_{\mathrm{ab}} - ES)^2 \quad . \tag{2.18}$$

Here we can neglect ES due to S being infinitesimally small and insert Equations 2.11, 2.12 and 2.13

$$0 = \left(\frac{\hbar\Omega + \Delta}{2} - E\right)\left(\frac{\hbar\Omega - \Delta}{2} - E\right)\left(\frac{\Delta_0}{2}\right)^2 \tag{2.19}$$

leading us to the energy eigenvalues

$$E_{\mathrm{g,e}} = \frac{1}{2}\left(\hbar\Omega \pm \sqrt{\mathit{\Delta}^2 + \mathit{\Delta}_0^2}\right) \ . \tag{2.20}$$

We earlier introduced the energy splitting as the difference between the energy of the ground and excited state and it can now be calculated as

$$E = E_{\mathrm{e}} - E_{\mathrm{g}} = \sqrt{\Delta^2 + \Delta_0^2} \quad . \tag{2.21}$$

Now we want the wave function for the ground and excited state. For this it is useful to use the matrix formalism and depict the Hamilton in the eigenbasis of the uncoupled wells (ψ_a, ψ_b)

$$H_0 = \frac{1}{2}\begin{pmatrix} \mathit{\Delta} & -\mathit{\Delta}_0 \\ -\mathit{\Delta}_0 & -\mathit{\Delta} \end{pmatrix} \tag{2.22}$$

for convenience the constant term $\frac{\hbar\Omega}{2}$ was ignored. We use the method for change of basis to transform the hamiltion into the eigenbasis of the two level system

$$\mathcal{H}_0 = \frac{1}{2}\begin{pmatrix} E & 0 \\ 0 & -E \end{pmatrix} \ . \tag{2.23}$$

The transformation matrices are given by

$$R_\phi = \begin{pmatrix} \cos\phi & -\sin\phi \\ \sin\phi & \cos\phi \end{pmatrix} \quad \text{and} \quad R_\phi^{-1} = \begin{pmatrix} \cos\phi & \sin\phi \\ -\sin\phi & \cos\phi \end{pmatrix} \tag{2.24}$$

with the rotation angle $\phi = \frac{1}{2}\arctan(\frac{\Delta_0}{\Delta})$. This gives us the the wave function for the ground and excited state depicted in Figure 2.4

$$\Psi_{\mathrm{g}} = \cos(\phi)\psi_{\mathrm{a}} + \sin(\phi)\psi_{\mathrm{b}} \tag{2.25}$$

$$\Psi_{\mathrm{e}} = \cos(\phi)\psi_{\mathrm{b}} - \sin(\phi)\psi_{\mathrm{a}} \ . \tag{2.26}$$

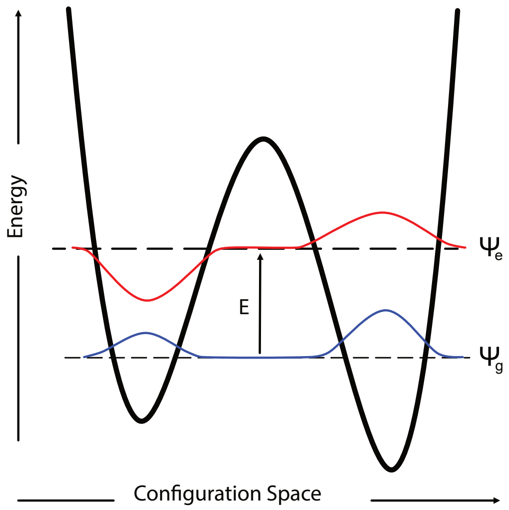

Figure 2.4: Depiction of the ground state Ψ_g and excited state Ψ_e inside the double well, with a difference in energy splitting E. Adapted from [Fre16].

2.3.2 Coupling Between Two Level Systems and External Fields

Without any disturbances our two level system parameters can be assumed to be constant. If we change our environment via application of a slowly varying field, the dipole moments of the tunneling systems couple to the external electric field leading to a small change in Δ and Δ_0. The same effect can be achieved by bending the sample slightly, inducing a strain field, that modifies the binding angle and length, and thus the asymmetry energy Δ, because of the deformation. For the following discussion it is thus only referred to as external field. If we follow the assumption that the changes are small we can use the first order perturbation theory to establish the perturbation Hamilton

$$H_{\mathrm{p}} = \frac{1}{2}\begin{pmatrix} \delta\varDelta & -\delta\varDelta_0 \\ -\delta\varDelta_0 & -\delta\varDelta \end{pmatrix} \tag{2.27}$$

in the basis of the single well. The change in barrier height V and distance d is negligible and we can approximate $\delta\Delta_0$ to be zero [Phi81, Lis15, Sar16]. We can use the transformation matrices we used in Equation 2.24 to transform the Hamiltonian in to the eigenbasis of the two level system resulting in

$$\mathcal{H}_{\mathrm{p}} = \frac{1}{2E}\begin{pmatrix} \varDelta & \varDelta_0 \\ \varDelta_0 & -\varDelta \end{pmatrix} \delta\Delta \quad . \tag{2.28}$$

Combining the undisturbed Hamilton with the perturbation Hamiltonian gives us

$$\mathcal{H} = \frac{1}{2}\begin{pmatrix} E & 0 \\ 0 & -E \end{pmatrix} + \frac{1}{E}\begin{pmatrix} \mathit{\Delta} & \mathit{\Delta}_0 \\ \mathit{\Delta}_0 & -\mathit{\Delta} \end{pmatrix} \delta\Delta \quad . \tag{2.29}$$

By combining the diagonal elements we can derive a change in energy splitting δE due to the change in asymmetry energy.

$$\delta E = \frac{\Delta}{E}\delta\Delta \quad . \tag{2.30}$$

The change in asymmetry energy is dependent on the field we apply. In the case of an electric field the determining factors are the dipole moment p and the field strength of the applied field F giving us the change

$$\delta\Delta = 2\vec{p}\vec{F} \quad . \tag{2.31}$$

In the case of an applied strain field the change depends on the strength of our field $\widetilde{e}$ which increases the more the length of our sample changes due to bending and the deformation potential γ, which is a measurement of the coupling strength between phonon and tunneling system.

$$\delta\Delta = 2\gamma\widetilde{e} \quad . \tag{2.32}$$

2.3.3 Relaxation Processes

Using the framework we discussed in Section 2.2, at low temperatures most systems reside in their ground state. If an electric field is applied, the energy splitting E changes due to the dipole moment $\vec{p}$ of a single system, thus the polarization P of the whole system is modified. This effect can lead to an excitation of the respective tunneling system, ripping them out of their thermal equilibrium, due to the change $\delta\Delta N$ in occupation number. In the limit of small fields $\vec{p}\vec{F} \ll k_B T$ the change in occupation number is directly proportional to the change in polarization

$$\delta P \propto \delta(\mathit{\Delta} N) \quad . \tag{2.33}$$

Naturally the systems want to return to their equilibrium state by emitting or absorbing thermal phonons. We can use the relaxation ansatz to get the change in polarization over time, while the system returns to its equilibrium value P_∞ with a constant relaxation time τ_1

$$\frac{\mathrm{d}P(t)}{\mathrm{d}t} = -\frac{P(t) - P_\infty(t)}{\tau_1} \quad . \tag{2.34}$$

For alternating electric fields the same equation can be achieved by applying the Debye formalism [Deb13]. By inserting Equation 2.1 we can link the polarization to the dielectric susceptibility resulting in

$$\chi(\omega) = \frac{\chi(0)}{1 - \mathrm{i}\omega\tau_1} \quad . \tag{2.35}$$

$\chi(0)$ can be obtained if we differentiate the polarization P from Equation 2.1 by the electric field F:

$$\chi(0) = \frac{1}{\varepsilon_0}\frac{\partial P}{\partial F} = \frac{p^2}{\varepsilon_0 k_\mathrm{B} T}\frac{\Delta^2}{E^2}\operatorname{sech}^2\left(\frac{E}{2k_\mathrm{B}T}\right) \quad . \tag{2.36}$$

Merging Equations 2.35 and 2.36 and splitting up the dielectric susceptibility into its real- and imaginary parts gives us the equations

$$\delta\varepsilon'_\mathrm{rel} = \frac{p^2\cos^2\theta}{\varepsilon_0 k_\mathrm{B}T}\left(\frac{\Delta}{E}\right)^2\operatorname{sech}^2\left(\frac{E}{2k_\mathrm{B}T}\right)\frac{1}{1+\omega^2{\tau_1}^2} \tag{2.37}$$

$$\delta\varepsilon''_\mathrm{rel} = \frac{p^2\cos^2\theta}{\varepsilon_0 k_\mathrm{B}T}\left(\frac{\Delta}{E}\right)^2\operatorname{sech}^2\left(\frac{E}{2k_\mathrm{B}T}\right)\frac{\omega\tau_1}{1+\omega^2{\tau_1}^2} \quad . \tag{2.38}$$

The frequency dependence of the real an imaginary part can be seen in Figure 2.5. As introduced in Section 2.1 the real part ε' accounts for energy storing processes. At low frequencies $\omega\tau_1 \ll 1$ the electric fields alternates slow enough, so that the dipole moments can easily follow in alignment to the field and energy can be sufficiently stored. For frequencies $\omega\tau_1 \approx 1$ the excitation becomes to fast in comparison to relaxation times for the system to completely follow the alignment and the system lags behind in phase. The real part decreases accordingly until the field changes so rapidly that our system becomes static and the real part approaches zero.

The imaginary part ε'' contains dissipation processes and start at zero for low frequencies while slowly increasing and reaching its peak at $\omega\tau_1 = 1$ since the most energy dissipates, due to the system lagging behind the field. Since at high frequencies the system becomes static no energy can be lost and the imaginary part drops to zero again. Relaxation processes in amorphous solids below temperatures of $T = 10\,\mathrm{K}$ occur by emission or absorption of thermal phonons. At lowest temperatures $T \leq 1\,\mathrm{K}$ only single phonons are emitted when relaxation to the ground state happens. This happens with the rate [Jä72]

$$\tau_{1P}^{-1} = \frac{\Delta_0}{E}\frac{E^3}{K_{1P}}\coth\left(\frac{E}{k_\mathrm{B}T}\right) \tag{2.39}$$

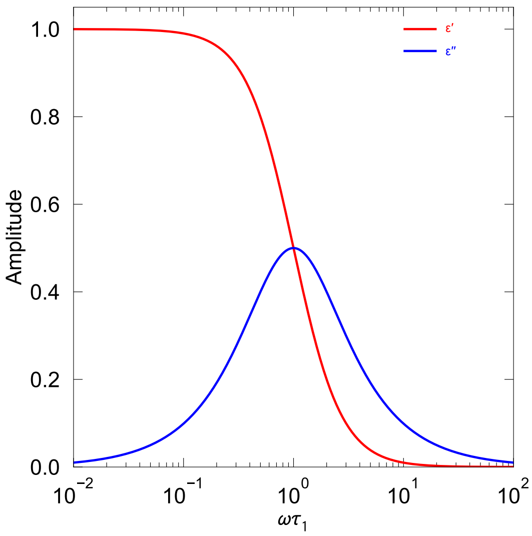

Figure 2.5: Normalized real (ε') and imaginary (ε'') contribution of a single two level system to the dielectric function by relaxation processes as a function over $\omega\tau_1$. Here ω is the frequency of the electric field and τ_1 the single phonen relaxation time.

with the coupling constant

$$K_{1\mathrm{P}} = 2\pi\rho\hbar^4 \left(\frac{\gamma_1^2}{\nu_1^5} + 2\frac{\gamma_\mathrm{t}^2}{\nu_\mathrm{t}^5}\right)^{-1} \quad . \tag{2.40}$$

Here ρ represents the mass density, ν is the sound velocity and γ the coupling strength of the longitudinal and transversal phonons. Since $E = \sqrt{\Delta^2 + \Delta_0^2}$ we can deduce that the relaxation times decreases if the energy minima of each well are close to each other with the fastest time achieved by symmetrical wells. At temperatures of about $T = 2K$ the number of thermal phonons increases to a point were two phonon relaxation processes become relevant as calculated by [Dou80] with the coupling constant K_{2P} for two phonon relaxation

$$\tau_{2\mathrm{P}} = K_{2\mathrm{P}} \frac{\Delta_0^2}{E^2} T^7 f \frac{E}{2k_\mathrm{B}T} \tag{2.41}$$

resulting in the total relaxation time

$$\tau_1^{-1} = \tau_{1\mathrm{P}}^{-1} + \tau_{2\mathrm{P}}^{-1} \quad . \tag{2.42}$$

2.3.4 Resonant Processes

If the energy of a photon matches the energy splitting $E = \hbar\omega_\mathrm{TS}$ of a two-level system $\hbar\omega = \hbar\omega_\mathrm{TS}$ they interact with each other. If the system resides in its ground state, the photon is absorbed, raising it to the excited state. However, if it resides in

the excited state, a second photon is emitted with the same energy, and the system changes to the ground state.
At high temperatures $k_\mathrm{B}T \gg \hbar\omega$ the population difference ΔN approaches zero and an equal amount of emission and absorption processes takes place, meaning resonant interactions are negligible and only become important at low temperatures where the population difference is high. The change in the dielectric function due to resonant processes can be calculation using Fermis golden rule again, as was done by [Car94] leading to the equations

$$\delta\chi'_{res} = \delta\varepsilon'_{res} = \frac{p^2\cos^2(\theta)}{\varepsilon_0\hbar}\left(\frac{\Delta_0}{E}\right)^2 \tanh\left(\frac{E}{2k_BT}\right) b'(w) \tag{2.43}$$

$$\delta\chi''_\mathrm{res} = \delta\varepsilon''_\mathrm{res} = \frac{p^2\cos^2(\theta)}{\varepsilon_0\hbar}\left(\frac{\Delta_0}{E}\right)^2 \tanh\left(\frac{E}{2k_BT}\right) b''(w) \tag{2.44}$$

using the frequency dependency

$$b'(w) = \frac{(\omega+\omega_\mathrm{TS})\tau_2^2}{(\omega+\omega_\mathrm{TS})\tau_2^2+1} - \frac{(\omega-\omega_\mathrm{TS})\tau_2^2}{(\omega-\omega_\mathrm{TS})\tau_2^2+1} \tag{2.45}$$

$$b''(\omega) = \frac{\tau_2}{(\omega-\omega_\mathrm{TS})^2\tau_2^2+1} - \frac{\tau_2}{(\omega+\omega_\mathrm{TS})^2\tau_2^2+1} \quad . \tag{2.46}$$

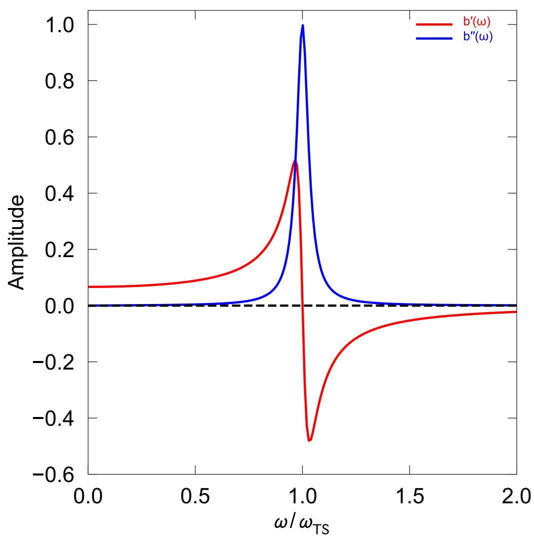

Figure 2.6: Normalized real (b') and imaginary (b'') contribution of a single two level system to the dielectric function by resonant processes as a function over $\frac{\omega}{\omega_0}$. ω_{TS} is the resonant frequency of our system.

Here τ_2 describes the transversal relaxation time, which describes the process of an excited system interacting with its neighboring systems, which dephases our initial system, leading to a loss of its coherence to the electrical field. Figure 2.6 shows how the real and imaginary part change as a function of frequency. At low frequencies $w \ll \omega_\mathrm{TS}$ there is a small positive contribution to the real part due to shifts in the dipole moment, while the imaginary part remains zero. At resonance $w = \omega_{\mathrm{TS}}$ the real part rises until it undergoes a sign change adding a negative contribution to the real part. The imaginary part rises sharply due to photons coupling with the tunneling systems and thus energy being dissipated from the electric field. At high frequencies the polarization becomes static leading the real part to approach zero with no negative contributions anymore. The imaginary part does the same since no resonant interaction with the tunneling system can take place and no energy being lost.

2.3.5 Parameter Distribution

The standard tunneling model makes two key assumptions: The first one is that the parameters Δ and λ are independent of each other and the second that the parameters are uniformly distributed. With this we can establish the distribution function with the material constant P_0 as

$$P(\varDelta, \lambda)\mathrm{d}\varDelta\mathrm{d}\lambda = P_0\mathrm{d}\varDelta\mathrm{d}\lambda \quad . \tag{2.47}$$

We can then transform the variables to get the distribution in terms of the coupling energy Δ_0 and the energy splitting E:

$$P(\Delta, \Delta_0) = P(\Delta, \lambda)|\frac{\partial\lambda}{\partial\Delta_0}|\mathrm{d}\Delta\mathrm{d}\Delta_0 = \frac{P_0}{\Delta_0}\mathrm{d}\Delta\mathrm{d}\Delta_0 \tag{2.48}$$

$$P(E, \varDelta_0)\mathrm{d}E\mathrm{d}\varDelta_0 = P_0|\frac{\partial\Delta}{\partial E}|\mathrm{d}E\mathrm{d}\varDelta_0 = P_0\frac{E}{\varDelta_0\sqrt{E^2 - \varDelta^2}}\mathrm{d}E\mathrm{d}\varDelta_0 \quad . \tag{2.49}$$

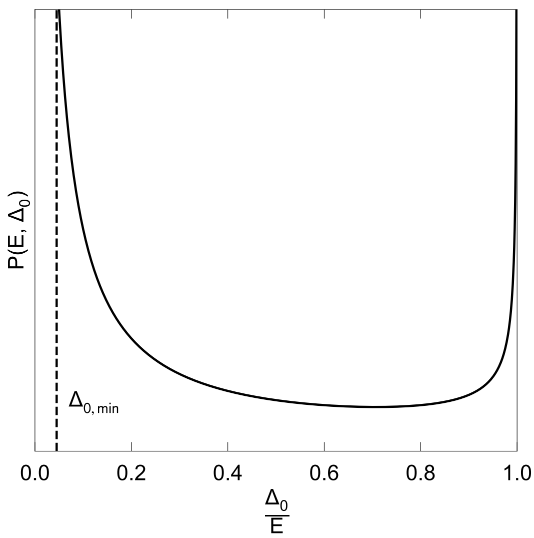

Figure 2.7: Distribution function of the parameters of a two level system in regards to the energy splitting E and coupling energy Δ_0. The minimum $\varDelta_{0,\mathrm{min}}$ which we need in order to integrate over the distribution is marked by the dotted line.

As can be seen in Figure 2.7 two singularities are present at $\Delta_0 = 0$ and $\Delta_0 = E$. We can integrate our function at the latter, while we need to introduce a minimum tunneling splitting $\Delta_{0,\mathrm{min}}$ in order to avoid non physical behavior at $\Delta_0 = 0$. Tunneling systems with tunneling splitting below $\Delta_{0,\mathrm{min}}$ can be understood as systems with a vanishing tunneling probability and each well can be considered isolated. We will use $\mathit{\Delta}_{0,\mathrm{min}} \lesssim 10^{-3} k_\mathrm{B} T_\mathrm{min}$ as found by [Luc16] with T_min the minimal temperature within the experiment .

2.3.6 Temperature Dependency

To model the temperature dependency of the dielectric function, we integrate the dielectric susceptibility of the relaxation and resonant contributions as seen in the Equations 2.37, 2.38, 2.43 and 2.44 with the parameter distribution shown in Equation 2.49 and the singularities $\Delta_{0,\ \mathrm{min}}$ and E as start and end points of the integrals. The results of these numerically calculated integrals can be seen in Figure 2.8, where we used a frequency of 1 GHz for the electric field.

Relaxation:

$$\frac{\delta\varepsilon'}{\varepsilon'} = \frac{1}{3\varepsilon_0\varepsilon'}\frac{p_0^2 P_0}{k_B T}\int_{\Delta_{0,\mathrm{min}}}^{E_\mathrm{max}} \mathrm{d}E \int_{\Delta_{0,\mathrm{min}}}^{E} \mathrm{d}\Delta_0 \left(1 - \frac{\Delta_0^2}{E^2}\right) \mathrm{sech}^2\left(\frac{E}{2k_B T}\right) \frac{1}{1+\omega^2\tau_1^2} \frac{E}{\Delta_0\sqrt{E^2-\Delta_0^2}} \tag{2.50}$$

$$\frac{\delta\varepsilon''}{\varepsilon''} = \frac{1}{3\varepsilon_0\varepsilon'}\frac{p_0^2 P_0}{k_B T}\int_{\Delta_{o,\mathrm{min}}}^{E_\mathrm{max}} \mathrm{d}E \int_{\Delta_{0,\mathrm{min}}}^{E} \mathrm{d}\Delta_0 \left(1 - \frac{\Delta_0^2}{E^2}\right) \mathrm{sech}^2\left(\frac{E}{2k_B T}\right) \frac{\omega\tau_1^2}{1+\omega^2\tau_1^2} \frac{E}{\Delta_0\sqrt{E^2-\Delta_0^2}} \tag{2.51}$$

The influence of relaxation effects depends on the relaxation time τ_1 and increases as it gets shorter. The relaxation time in turn correlates to the number of available thermal phonons. At low temperatures this number is low and thus the relaxation time is high, leading to negligible contributions for both the real and imaginary part. At $T \approx 1K$ tunneling systems with relaxation times of $\omega\tau_1 < 10$ start to appear, resulting in a rise of the real part, while the imaginary part starts to rise slightly earlier. At high temperatures the real part increases steadily as more systems can contribute with the decrease in relaxation time. The imaginary parts however flattens into a plateau since only tunneling system with $\omega\tau_1 \approx 1$ contribute.

Resonance:

$$\frac{\delta\varepsilon'}{\varepsilon'} = \frac{1}{3\varepsilon_0\varepsilon'}\frac{p_0^2 P_0}{k_B T}\int_{\Delta_{o,min}}^{E_{max}} \mathrm{d}E \int_{\Delta_{o,min}}^{E} \mathbf{d}\Delta_0 \frac{\Delta_0^2}{E^2} \tanh\left(\frac{E}{2k_B T}\right) b'(w) \frac{E}{\Delta_0\sqrt{E^2-\Delta_0^2}} \tag{2.52}$$

$$\frac{\delta\varepsilon''}{\varepsilon''} = \frac{1}{3\varepsilon_0\varepsilon'}\frac{p_0^2 P_0}{k_B T}\int_{\Delta_{0,\min}}^{E_{\max}} \mathrm{d}E \int_{\Delta_{\mathrm{o},\min}}^{E} \mathrm{d}\Delta_0 \frac{\Delta_0^2}{E^2}\tanh\left(\frac{E}{2k_BT}\right) b''(w)\frac{E}{\Delta_0\sqrt{E^2-\Delta_0^2}} \tag{2.53}$$

The real part contribution of resonant processes is small at high temperatures, since the population difference between ground and excited state is nearly zero and only systems with $w \ll w_{TS}$ are not fully thermally saturated and can contribute because of dipole shifts as explained in Section 2.3.4. As the temperature decreases, more systems with lower frequencies are no longer saturated leading to an increase in the real part. This leads to a maximum at a temperature of around 30mK, which decreases slightly at even lower temperatures because more systems with frequencies $w \geq \omega_{\mathrm{TS}}$ are available and these contribute negatively to the real part due to the sign change at $\omega = \omega_{\mathrm{TS}}$. This negative contribution quickly approaches to zero leading to a plateau at lowest temperatures.
For the imaginary part the contribution consists only of resonant tunneling systems with frequencies $\omega \approx \omega_{\mathrm{TS}}$. Because of this, the imaginary part starts of at zero for high temperatures, as all systems in this range are saturated. When the temperature reduces to a point where resonant system become available, the resonant contribution begins to rise continuously until it stays constant at $T \approx 10\,\mathrm{mK}$ because all resonant systems are fully able to contribute.

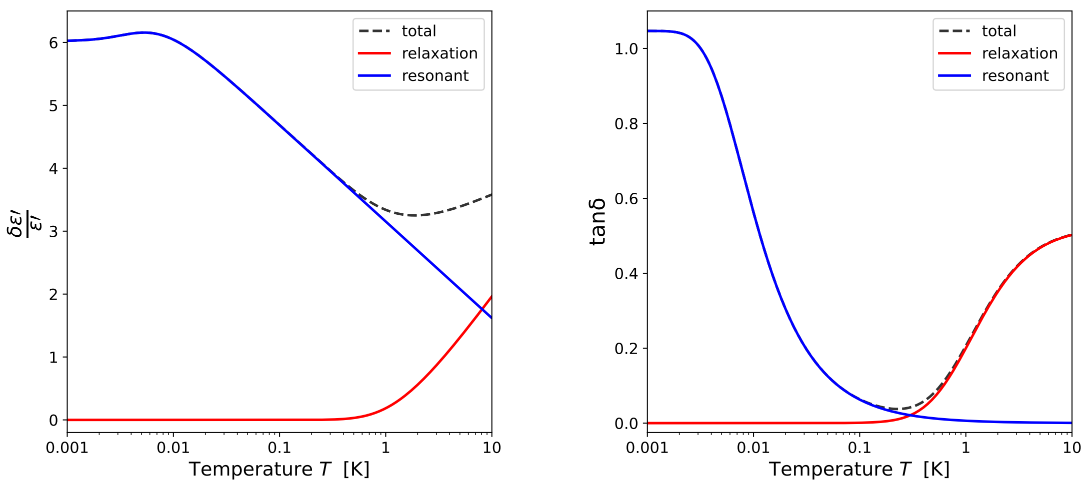

Figure 2.8: Temperature dependency of the dielectric function with the real part on the left and the imaginary part on the right, while an electric field with the frequency $\mathrm{f} = 1\,\mathrm{GHz}$ is applied. In both cases are the resonant contributions dominant at low temperatures while at higher temperatures the relaxation is the relevant contributor. Data from [Fre21]

Combining these results, we can see that at low temperatures resonant contributions dominate due to low saturation of tunneling system and a small amount of thermal phonons. This changes at higher temperatures until relaxation processes become dominant, with a minimum in the real part proportional to the relaxation time $T_{\mathrm{min}} \propto \tau_1$.

2.4 Landau-Zener Loss

In this section we discuss the dielectric loss of glass at low temperatures under the influence of an additional mechanical strain field, also called bias field. We have shown earlier, that external fields have the ability to modulate the energy splitting of a tunneling system. The strain-field applied is supposed to be stronger than the probe field $F_{\mathrm{probe}} \ll F_{\mathrm{bias}}$ so that the effect of the probe field on the energy splitting can be ignored.

$$E(t) = \sqrt{\Delta_0^2 + (\Delta + \delta\Delta(t))^2} \quad . \tag{2.54}$$

As seen in section 2.3.4 and 2.3.6, the only contributor to the dielectric loss at low temperatures are tunneling systems with energy splitting near resonance due to the resonant interaction from photons with two-level systems of similar energy. For this reason we can use the Taylor approximation for $\delta\Delta \to 0$ to get

$$E(t) \approx E_0 + \sqrt{1 - \left(\frac{\Delta_0}{E_0}\right)^2}\delta\Delta(t) \tag{2.55}$$

with $E_0 = \sqrt{\Delta^2 + \Delta_0^2}$ the energy splitting before modulation. Inspecting the change in energy over time, we can define the energy bias rate ν as

$$\hbar\nu = \frac{\mathrm{d}E(t)}{\mathrm{d}t} = \sqrt{1 - \left(\frac{\Delta_0}{E_0}\right)^2}\delta\dot{\Delta}(t) \tag{2.56}$$

and if we differentiate Equation 2.32 we can insert it into this framework

$$\hbar\nu = \sqrt{1 - \left(\frac{\Delta_0}{E_0}\right)^2} 2\gamma\dot{\tilde{e}} = \hbar\nu_0\sqrt{1 - \left(\frac{\Delta_0}{E_0}\right)^2} \tag{2.57}$$

with $\nu_0 = \frac{2\gamma\dot{\tilde{e}}}{\hbar}$. It should be mentioned that for matters concerning the bias field, the deformation potential γ is used, whereas for matters of the probe field the dipole moment p must be used. If we assume the change in energy splitting to be linear, achieved by a linear bias ramp, we get

$$E(t) = \hbar\omega + \hbar\nu(t - t_0) \tag{2.58}$$

where t_0 is the time at which the tunneling system interacts resonantly with the

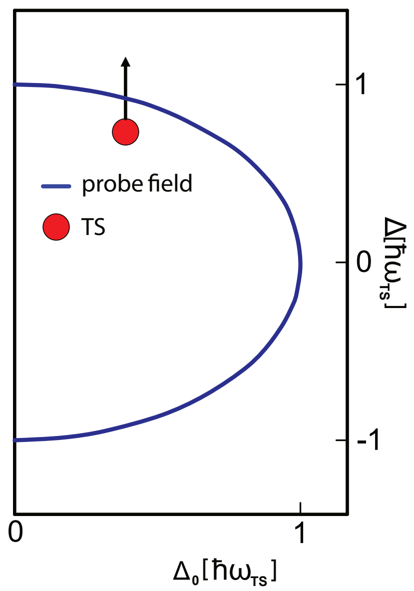

Figure 2.9: Schematic representation of a single tunneling system changing its asymmetry energy Δ due to an applied bias field and crossing the resonant frequency because of this change. The tunneling system is represented by a red dot, while the frequency of probe field is symbolized with a blue semi circle. Adapted from [Bli22].

probe field $\hbar\omega = E$. The visualization of this process can be seen in Figure 2.9. Tunneling systems with resonant energy splitting, so the right ratio of Δ and Δ_0, as marked by the blue circle, are subject to resonant interactions with the driving field, while our bias field changes the energy splitting and pushes new tunneling systems over this circle. The energy splitting can change positively and negatively, meaning that different tunneling systems can cross the resonance frequency everywhere on the circle along the Δ axis with the same probability, due to the uniform distribution of our parameters.

Considering this we want to get the probability of our system being either in the ground or excited state. For this we use the wave function $|\Psi(t)\rangle = c_{\mathrm{g}}(t)\,|\Psi_{\mathrm{g}}\rangle + c_{\mathrm{e}}(t)\,|\Psi_{\mathrm{e}}(t)\rangle$ with c_{g}, c_{e} the probability amplitude of the respective state and solve the time dependent Schrödinger equation

$$i\hbar\frac{\partial}{\partial t}|\Psi\rangle = \mathcal{H}\,|\Psi\rangle \tag{2.59}$$

with the Hamiltonian from Equation 2.29. In the solution we neglect relaxation effects and assume the effect of the driving field to be small $\frac{E}{2} \gg \frac{\Delta}{E}pF_{\mathrm{ac}}$ resulting in the differential equations

$$\mathrm{i}\hbar\dot{c_{\mathrm{e}}}(t) = \frac{E}{2}c_{\mathrm{e}}(t) + \hbar\Omega_{\mathrm{R}}\cos(\omega t)c_{\mathrm{g}}(t) \tag{2.60}$$

$$\mathrm{i}\hbar\dot{c_{\mathrm{g}}}(t) = -\frac{E}{2}c_{\mathrm{g}}(t) + \hbar\Omega_{\mathrm{R}}\cos(\omega t)c_{\mathrm{e}}(t) \tag{2.61}$$

were the Rabi frequency Ω_R is introduced. It gives us the oscillation between the ground- and excited state because of the driving field and is given by

$$\Omega_\mathrm{R} = \frac{\Delta_0}{E}\frac{pF_\mathrm{ac}}{\hbar}\cos\theta = \frac{\Delta_0}{E}\Omega_{\mathrm{R},0}\cos\theta \tag{2.62}$$

with $\Omega_{\mathrm{R},0} = \frac{pF_\mathrm{ac}}{\hbar}$. It is important to note that originally the Landau-Zener dynamics were introduced with an electric bias field in mind and thus θ is the angle between electrical bias field and dipole moment of a single tunneling system. It quantifies if the change $\delta\Delta$ is positive or negative and by which factor it is changed. θ follows the universal distribution as explained in Section 2.3.5 and thus the factor for the change $\delta\Delta$ follows suit. Since this is also the case for acoustic biasing the same mathematical framework can be used.

Going back to our differential equations, we can transform those into a rotating frame with $(a_\mathrm{e}, a_\mathrm{g}) = (c_\mathrm{e}\exp(\frac{\mathrm{i}\omega t}{2}), c_\mathrm{g}\exp(\frac{-\mathrm{i}\omega t}{2}))$ and take advantage of the rotating wave approximation to get

$$\dot{a_\mathrm{e}}(t) = -\frac{\mathrm{i}\nu}{2}(t-t_0)a_\mathrm{e} - \frac{\mathrm{i}\Omega_\mathrm{R}}{2}a_\mathrm{g} \tag{2.63}$$

$$\dot{a_\mathrm{g}}(t) = \frac{\mathrm{i}\nu}{2}(t-t_0)a_\mathrm{g} - \frac{\mathrm{i}\Omega_\mathrm{R}}{2}a_\mathrm{e} \quad . \tag{2.64}$$

These equations match the equations of the Landau-Zener problem for a two-level system [Lan32, Zen32].

A tunneling system at low temperature is assumed to be in the ground state. If it undergoes a change in energy splitting resulting in it being swept through the resonant energy, it can either resonantly absorb a photon or cross while remaining in the ground state, which is called Landau-Zener transition. By solving the equations we get the probability for this transition to happen

$$|a_\mathrm{g}|^2 = P_\mathrm{LZ} = \exp\left(-\frac{\pi\Omega_\mathrm{R}^2}{2\nu}\right) = \exp(-\delta) \quad . \tag{2.65}$$

We can see that at slow bias rates $\dot{F}_\mathrm{bias}$ the chance of a photon being resonantly absorbed is high, while at higher rates a Landau-Zener transition becomes more likely. To calculate how much energy is dissipated due to resonant absorption, we need to integrate over the number of all relevant tunneling system with the transition energy $\hbar\omega$ and the probability of a resonant absorption $P = 1 - P_\mathrm{LZ}$ resulting in

$$\mathrm{d}E_\mathrm{dis} = \int \mathrm{d}V \int \mathrm{d}N\hbar\omega P \tag{2.66}$$

with the sample Volume V. Inserting the distributions for tunneling system parameters leads us to

$$\mathrm{d}E_{\mathrm{dis}} = \hbar\omega P_0 V \int_0^1 \mathrm{d}\cos\theta \int_0^{\hbar\omega} \mathrm{d}\Delta_0 \int_{\hbar\omega-\hbar\nu\mathrm{d}t}^{\hbar\omega+\hbar\nu\mathrm{d}t} \mathrm{d}E \frac{(1-\exp(-\delta))E}{\Delta_0\sqrt{E^2-\Delta_0^2}} \quad . \tag{2.67}$$

We can further approximate this by assuming small changes in energy $\hbar\nu\mathrm{d}t \ll \hbar\omega$, substituting $x = \frac{\Delta_0}{\hbar\omega}$ and use the Taylor approximation [Fre21], giving us the dissipated power

$$P_{\mathrm{dis}} = \frac{\mathrm{d}E_{\mathrm{dis}}}{\mathrm{d}t} = \pi\omega V P_0 p^2 F_{\mathrm{ac}}^2 \int_0^1 \mathrm{d}\cos\theta\cos^2\theta \int_0^1 \mathrm{d}x \frac{1-e^{-\delta}}{\delta}\frac{1}{\sqrt{-x^2}} \quad . \tag{2.68}$$

We are now able to define the loss tangent as dissipated power per cycle and stored energy $W_{\mathrm{tot}} = \varepsilon_0\varepsilon_{\mathrm{r}}F_{\mathrm{ac}}^2 V$

$$\tan\delta = \frac{P_{\mathrm{dis}}}{\omega W_{\mathrm{tot}}} \tag{2.69}$$

which we can further rewrite for high bias rates were the approximation $e^{-\delta} = 1-\delta$ is valid to get a constant loss

$$\tan\delta_0 = \frac{\pi P_0 p^2}{3\varepsilon_0\varepsilon_{\mathrm{r}}} \quad . \tag{2.70}$$

This is also a good point to introduce the dimensionless bias rate, with the goal to simplify comparisons of the loss at different driving field strengths

$$\xi = \frac{2\nu_0}{\pi\Omega_{\mathrm{R},0}^2} \quad . \tag{2.71}$$

Uniting the last 4 equations gives us our final expression for the loss tangent for which the numerical solution can be seen in Figure 2.10

$$\tan\delta = 3\tan\delta_0\xi \int_0^1 \mathrm{d}\cos\theta\cos\theta \int_0^1 \frac{\mathrm{d}x}{x}\left(1-\exp\left(-\frac{\cos\theta}{\xi}\frac{x^2}{\sqrt{1-x^2}}\right)\right) \quad . \tag{2.72}$$

We need to be careful in interpreting this since we ignored relaxation effects in our calculations. For low bias rates our integral approaches zero because the energy splitting changes so slowly that emission and absorption of photons cancel each other. In reality however tunneling systems can relax back to the ground state given enough time, so the steady state limit introduced in Equation 2.7 marked by the red doted line takes over. As the bias rate increases, so does the dielectric loss since more new systems are able to resonantly interact with the driving field and our calculations become valid. This increase slows down at higher bias rates until it reaches the constant $\tan\delta_0$. At this point we sweep over the resonant crossing so

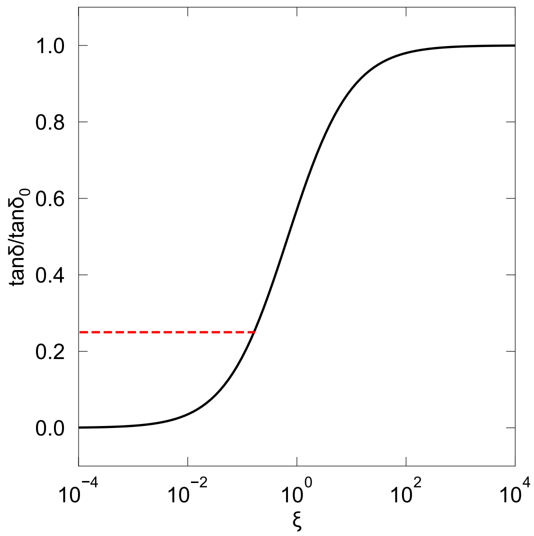

Figure 2.10: Numerical integration of the dielectric loss over the dimensionless bias rate of the bias field. The bias field changes the energy splitting while the driving field that is additionally applied interacts resonantly with the tunneling system. The red dotted line marks the steady state loss, were the bias rate is too slow to significantly impact the loss, with the result that it can be ignored. Data from [Bli22].

fast, that the probability of a photon being absorbed is low, so the effects of more tunneling systems being able to interact and the probability decreasing cancel each other out leading to the aforementioned plateau.

3. Experimental Methods

In this chapter, we introduce the setup we used to conduct out experiments. We start by shortly introducing the cryostat, followed up by the signal pathway. We then explain the resonator and composition of the sample on which the measurements will be conducted. We also show the acoustic biasing setup and the workings of a piezoelectric actuator. Finally, it is explained how the dielectric function is extracted from the measured data and how to obtain the acoustic bias rate.

3.1 Measurements at Low Temperature

We use a ^{3}He/^{4}He dilution refrigerator, which allows us to cool our sample down to temperatures below 10 mK. The glass is mounted to a sample holder that is attached to the experimental platform, which is thermally coupled to the mixing chamber, the coldest part within the cryostat. For a deeper understanding of the cooling principle, a read in [Ens05] is advised. To keep the sample at a stable temperature, a heater controlled by a PID-feedback controller is used. The temperature is measured with a carbon resistance thermometer[1]. The temperature we use in our setup is 30 mK because there the population difference is with $\Delta n = \tanh(\frac{E}{2k_{\mathrm{B}}T}) = 0.62$ high, while local heating effects, due to the experimental procedure, remain small enough. We need most systems in the ground state, because we want to study the resonant loss, while the sample is placed inside an electric driving field and this is only sensible at low temperature as discussed in Section 2.3.6.

3.2 Signal Pathway

In order to research dielectric behavior of the sample under the influence of a driving field, a microstructured LC-resonator on glass substrate is used. A radio frequency (rf-) signal stimulates the resonator. The readout is done with a vector network analyzer[2] (VNA), via coaxial cables. The VNA can supply signals in the range from 10 dBm to -30 dBm. The signal is then attenuated by a 30 dB attenuator, followed by an adjustable attenuator which can be adjusted in a range from 0 to 81 dB.

[1] AVS-47, RV-Elektroniikka Oy Picowatt, Veromiehentie 14, FI-01510 Vantaa, Finland

[2] R & S®ZNB8, Rohde & Schwarz GmbH & Co. KG, Mühldorfstraße 15, 81671 München, Germany

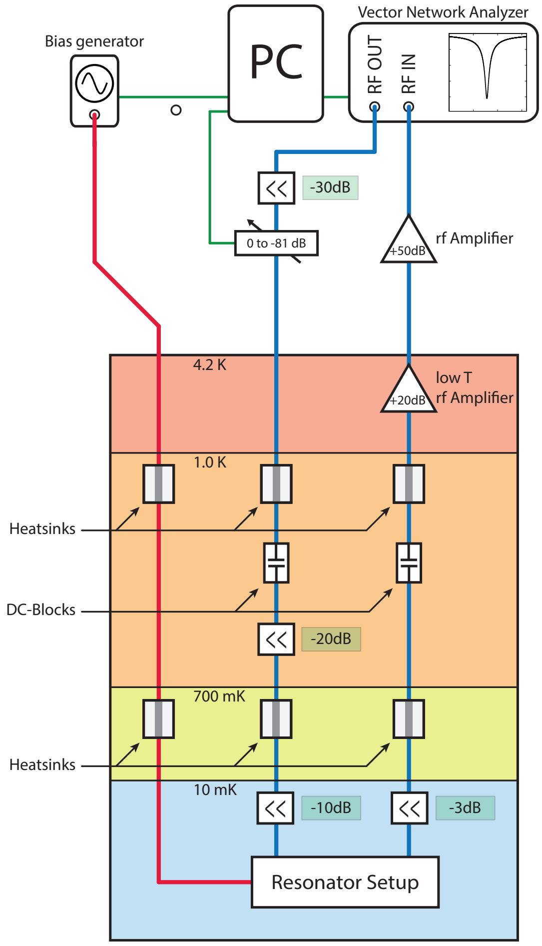

Figure 3.1: Illustration of the signal pathway. The box with the colored sections represents the pathway inside the cryostat, the rest is outside at room temperature. The blue lines represent the rf-signal pathway and the red line the connection between the bias generator and the PEA stack. Green is used for the pathways connecting the PC to the different parts. Adapted from [Sta25]

A LabView program[3] is used to control the VNA as well as the attenuator settings. Instead of solely relying on the adjustable attenuator, the 30 dBm attenuator is employed in order to reduce standing waves occurring due to differences in wave impedance of the coaxial cables.
Inside the cryostat, several heatsinks are used in order to thermally couple the cables to it and avoid heat input to colder stages of the cryostat. DC-blocks are used to filter out occurring DC-signals for the same purpose. Two additional attenuators, the first with 20 dB at a temperature of around 1 K and the second in the mixing chamber with 10 dB, are used to reduce the thermal noise entering our setup even further. After interacting with the resonator, the signal leaving through the heatsinks and DC-blocks has a very low amplitude. For this reason the signal is amplified by +20 dB with an low temperature rf-Amplifier still inside the cryostat and an additional 50 dB outside the cryostat. Since some noise is deflected back into the setup an additional attenuator at 3 dB is employed in the mixing chamber. For the bias signal, a simple

[3]LabView 8.5, National Instruments Corporation, 11500 N MopPax Expwy, Austin TX 787593504, USA

generator is used. It is connected to the resonator with coaxial cables, which only have heatsinks to reduce the thermal load acting on the mixing chamber.

3.3 Resonator and Sample

To study the dielectric response of amorphous solids we use an LC-resonator designed by [Sta25] with the software *Cadance*[4]. A meander line was used as an inductor connected to a microstructured interdigital capacitor (IDC) forming our resonator. The IDC consists of 80 fingers with 100 μm in length, 6 μm width an a distance of 2 μm between each finger. The ends of each finger are rounded in order to avoid non-linear behavior. Niobium sputter deposited directly on the glass sample is used to build the resonator and the feedline. The resonance frequency of the resonator

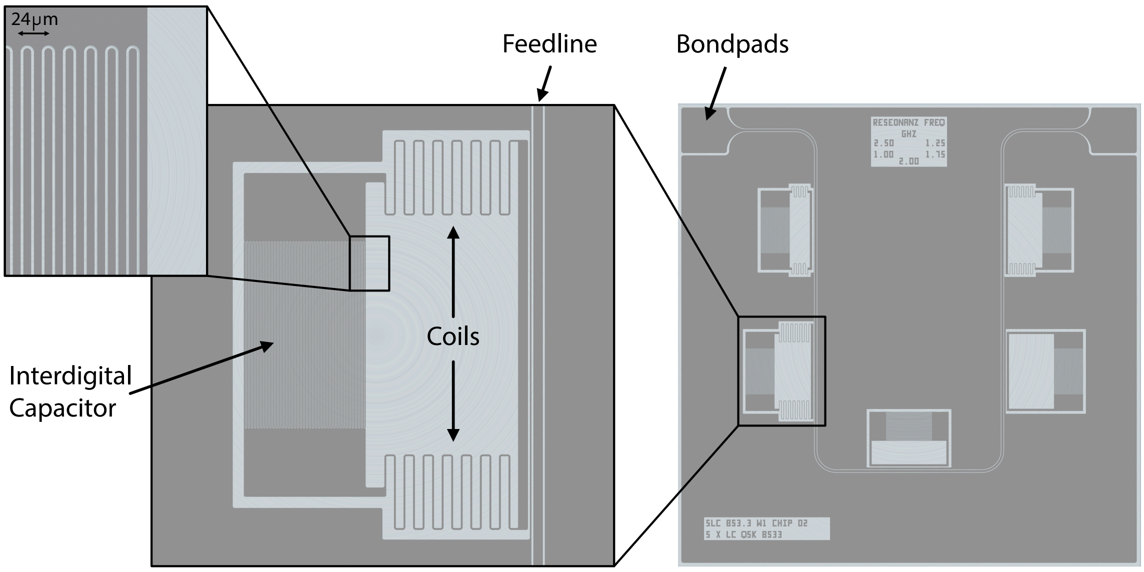

Figure 3.2: Illustration of the LC-resonator design used in this thesis. 4 Resonators with different resonance frequencies are sputtered on our BS 3.3 sample, while we will only use the resonator with a resonance frequency of 1.16 GHz for our measurements. The feedline, connected to coaxial via the bondpads, induces the resonator. The resonator itself consists of coils and the interdigital capacitor (IDC). Adapted from [Sta25].

is 1.16 GHz The whole setup is illustrated in Figure 3.2 and consists out of five different resonators with different resonance frequencies, but we will only use the one mentioned. We use niobium as our microstructure because at a temperature of $T = 9.2\,\mathrm{K}$ [Mat63] it gets superconducting and we can avoid ohmic losses which would heat our sample. The sample we use in order to study the dielectric response is

[4]Cadance Design Systems, 21 Oak Hill Ave, Endicott, NY 13760, USA

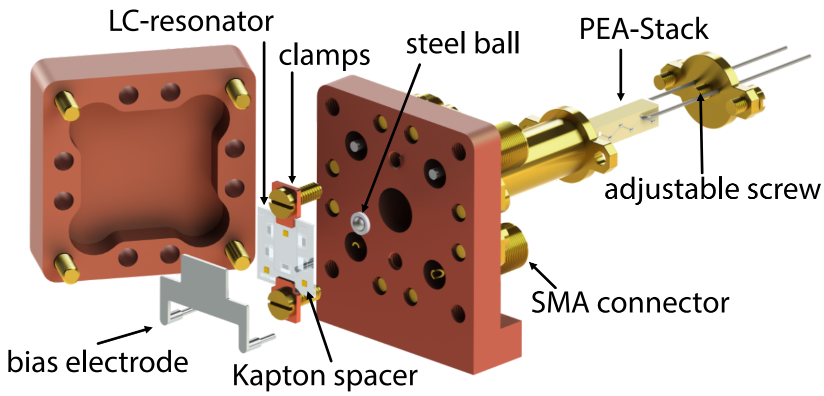

Figure 3.3: Render of the sample holder case with its parts. The resonator is placed inside the holder and a bias electrode hovers above it with Kapton spacers used to ensure a consistent distance. The rf-signal enters the holder through SMA connectors, which were bonded to the feedline. The PEA-stack is placed outside the holder and connects to the resonator through a small hole. A steel ball is placed between resonator and stack to have a single contact point. Adapted from [Sta25].

borosilicate glass BS 3.3[5] and features a relative permittivity of $\varepsilon_r = 4.6$. It consists mainly of silicon dioxide and boron trioxide. The whole chemical composition can be seen in table 3.1. The sample has a length and width of 10 mm and a thickness of 125 μm. The sample is clamped down to the sample holder made of oxygen-

SiO_2	B_2O_3	Na_2O	Al_2O_3	K_2O	BaO
83,4%	11,6%	3,4%	1,14%	0,41%	0,005%

Table 3.1: Chemical composition of BS 3.3

free copper. Copper is used due to its has good thermal conductivity. The inside of the sample holder is coated with niobium, which is for the sake of clarity not depicted, to reduce radiation losses of the resonator. The rf-signal enters the sample holder through SMA[6] connectors where the coaxial cables are attached to. The SMA connectors are bonded with aluminum wires to the bondpads, which establishes a connected between the VNA and the feedline. A bias electrode is placed above the resonator with Kapton[7] spacers in the middle to ensure a constant distance between the resonator and the electrode. The bias electrode is used for electrical biasing and plays no role in our measurements.

[5] Th. Geyer GmbH & Co. KG, Dornierstraße 4-6,71272, Renningen, Germany
[6] Sub-Miniature-A
[7] CMC 70125, DuPont, 974 Centre Rd., Wilmington, DE 19805, USA

3.4 Acoustic Biasing Setup

We have explained that the acoustic bias field is induced by bending the sample, leading to a change in properties. This is achieved in our setup with the use of a piezoelectric actuator[8] (PEA). It uses the principle of the inverse piezoelectric effect, where if certain solids are placed inside an electric field, they change their dipole alignment, leading to a change in bond angle, resulting in expansion or contraction of the piezoelectric material. To enhance this effect, multiple ceramic chips are stacked face-to-face with each other with electrodes in between. The commercially available stack we use employs chips consisting of lead zirconate titanate bonded together with epoxy and glass beads. The stack is connected to a signal generator. Experiments done by [Adh21] show that the maximum displacement at low temperatures is 1.2 μm with the maximum voltage of 75 V. It is important to note that our sample can heat up if it oscillates fast due to quick changes in voltage. They also found the maximum displacement at low temperatures is 1.2 μm at the maximum voltage of 75 V as seen in Figure 3.4. The PEA is fixed inside a brass tube, in order to ensure that the

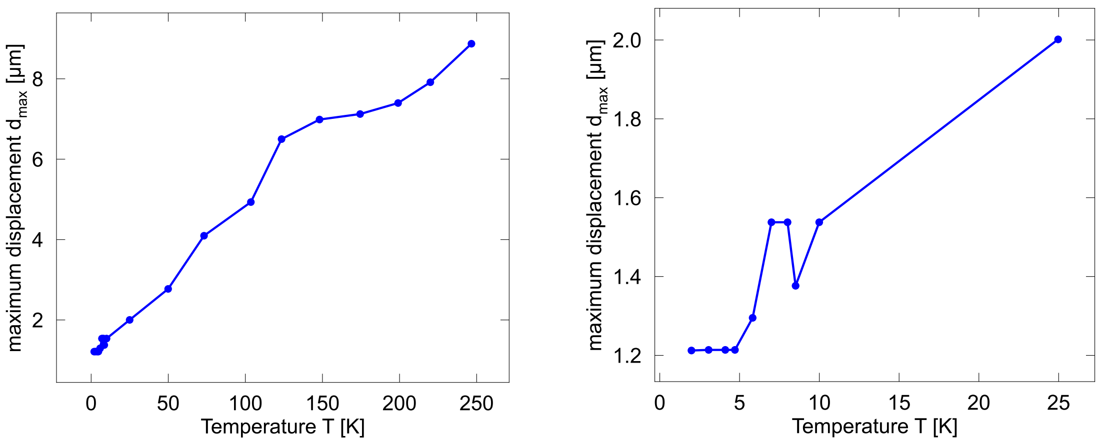

Figure 3.4: Plot of the maximum displacement of the PEA-stack at 75 V for different temperaturs. The right plot shows only the displacement for lowest temperatures and we can observe that for 5 K and lower the displacement remains at a constant 1.2 μm. Data from [Adh21].

position of the PEA is stable and connects to the resonator through a hole inside the sample holder. An additional stainless steal ball is placed between the PEA and our sample to establish a single contact point. In its neutral state with no voltage applied, the stack already presses slightly against the sample, resulting in a preload acting upon it. To ensure this, an adjustable screw is used to place the PEA in the right position. We will show that this preload has no effect on the loss and allows

[8] Type PK2FVP2, Thorlabs Inc., 43 Sparta Ave Newton, NJ 07860, USA

us to directly link the loss to the displacement of the PEA.

3.5 Measurement Principle

To study the dielectric response while an electric field is applied, we need to connect the dielectric function with the resonance frequency f_0 and the quality factor Q of the LC-resonator. The resonance frequency is given by

$$f_0 = \frac{1}{2\pi\sqrt{LC}} \tag{3.1}$$

with the inductance L and the capacitance C of the resonator. Power inside the LC-circuit is dissipated due the interaction with tunneling systems leading to a dampening in resonance amplitude and can thus be understood as a RLC-circuit with the resistance R

$$P_{\mathrm{dis}} = \frac{U_{\mathrm{ac}}^2}{2R} \quad . \tag{3.2}$$

As explained in Section 3.3 ohmic and radiation losses, which normally need to be considered, can be ignored due to the nature of our setup.
Combining these equations leads us to the intrinsic quality factor Q_{i}, defined as the ratio of energy stored inside the resonator $W_0 = \frac{1}{2}CU_{\mathrm{ac}}^2$ over the energy dissipation per cycle

$$Q_{\mathrm{i}} = 2\pi f_0 \frac{W_0}{P_{\mathrm{dis}}} = R\sqrt{\frac{C}{L}} \quad . \tag{3.3}$$

We need to take into account that the resonator is induced via a feedline with the coupling quality factor Q_{c} and add the inverse resulting in a reduction of the total quality factor

$$\frac{1}{Q} = \frac{1}{Q_{\mathrm{i}}} + \frac{1}{Q_{\mathrm{c}}} \quad . \tag{3.4}$$

We have shown in Sections 2.3.3 to 2.3.5 that at low temperatures the real part of the dielectric function changes in response to an applied electric field, because of resonant processes. Since the real part describes energy storing processes, the capacitance and with it the resonance frequency respond to changes in it. If we set C_{ref} and $f_{0,\mathrm{ref}}$ as arbitrary reference points we can get the relative change of the capacitance and by interesting Equation 3.1 the relative change of the resonance frequency

$$\frac{\Delta C}{C} = \frac{C - C_{\mathrm{ref}}}{C_{\mathrm{ref}}} = \left(\frac{f_{0,\mathrm{ref}}}{f_0}\right)^2 - 1 \quad . \tag{3.5}$$

Since the electric field also interacts with and probes the volume outside the sample we have to split up the capacitance into two parts, the capacitance of the sample C_{x}

and a parasitic stray capacitance C_p which we assume to be constant

$$C = C_\mathrm{x} + C_\mathrm{p} \quad . \tag{3.6}$$

We already linked changes in capacity to changes in the real part and can now narrow it to being directly proportional to the capacitance of the sample $C_\mathrm{x} \propto \varepsilon'$ and combining this with Equation 3.5 leads us to

$$\frac{\delta\varepsilon'}{\varepsilon'} = \frac{\Delta C_\mathrm{x}}{C_\mathrm{x}} = \frac{\Delta C}{C}\frac{1}{1-\frac{C_\mathrm{p}}{C}} = \left[\left(\frac{f_{0,\mathrm{ref}}}{f_0}\right)^2 - 1\right]\frac{1}{\mathcal{F}} \tag{3.7}$$

were we defined the filling factor $\mathcal{F} = 1 - \frac{C_\mathrm{p}}{C}$ as the ratio of energy stored in the sample and in the resonator as a whole. Since the internal quality factor is dependent on the capacitance, the parasitic stray capacitance also needs to be considered and taken out because we only want to research effects of the sample. This leads us to the quality factor of the sample $Q_\mathrm{TS} \approx Q_\mathrm{i,x}$ with the ratio $Q_\mathrm{i}/Q_\mathrm{i,x} = (C/C_\mathrm{x})^{\frac{1}{2}}$. If we compare the quality factor with Equation 2.69 of the loss tangent we can see that one is the inverse of the other giving us the relation

$$\tan\delta = \frac{1}{Q_\mathrm{i,x}} = \frac{1}{Q_\mathrm{i}\sqrt{\mathcal{F}}} \quad . \tag{3.8}$$

We now know how to obtain the real part from the resonance frequency and imaginary part from the quality factor and want to obtain those from the VNA readout signal S_{12}. We also have to consider external factors that influence our signal. One is the cable delay τ, another are possible impedance mismatches we account for with the complex quality factor $e^{\mathrm{i}\Phi}$ and phase shifts $e^{\mathrm{i}\alpha}$. Lastly we need to have an additional factor a since we amplify or attenuate our signal. This was already done by Probst *et al.* [Pro15] giving us the Equation for the non-ideal behavior of a notch-type resonator

$$S_{12}(f) = \frac{U_\mathrm{out}}{U_\mathrm{in}} = a e^{\mathrm{i}\alpha} e^{2\pi\mathrm{i}f\tau}\left(1 - \frac{Q/Q_\mathrm{c}e^{\mathrm{i}\Phi}}{1+2iQ\frac{f-f_0}{f_0}}\right) \quad . \tag{3.9}$$

If we use the Amplitude $|S_{21}|$ as a fit function for the measured resonance curves, we can finally obtain the desired values. An example of this fit can be seen in Figure 3.5.

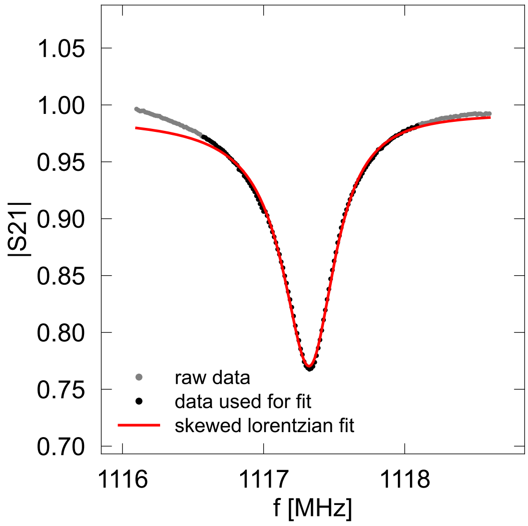

Figure 3.5: Example of a resonance curve, with its respective fitted function. The fit is shown in red, while the data points are shown in black and gray. Only the black points are used for the fit to ensure the closest fit during a resonance sweep.

3.6 Single Ramp Acoustic Biasing

The PEA is setup in a way that it presses against our sample, causing it to bend slightly, straining the sample, due to the difference in length between the neutral axis L and the outer scope L' of our sample due to the width $h = 0.2mm$, inducing a strain-field.

$$\widetilde{e} = \frac{\Delta L}{L} = \frac{L' - L}{L} \quad . \tag{3.10}$$

Like it can be seen in Figure 3.6, we assume our deformation to be circular, with the circle crossing the x-axis at the mounting points at $(\pm\frac{D}{2}, 0)$ with D the distance between our mounting points and the deflection at height $(0, z)$. The Radius of our circle is given by

$$R = \frac{z}{2} + \frac{D^2}{8z} \tag{3.11}$$

and for our setup we can take R·z to be constant at $12.5 \cdot 10^{-6} m^2$ and the relative changes as equal (See A.1).

$$\frac{\Delta R}{R} = -\frac{\Delta z}{z} \quad . \tag{3.12}$$

The calculations that led us to these equations can be further examined in Appendix A.1. With this in mind we can calculate the strain-field with Θ the corresponding angle of the circle cutout

$$L = \Theta R \quad \text{and} \quad L' = \Theta \left(R + \frac{h}{2} \right) \quad . \tag{3.13}$$

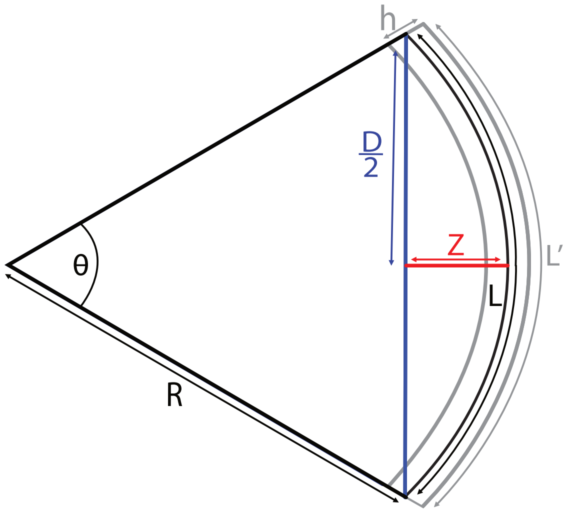

Figure 3.6: Illustration of the different chip parameters during bending. L is the neutral axis and L' the outside axis of the chip. The length of the chip without bending is D and the deflection is given by Z. The imagined circle we get by continuing the neutral axis has the radius R. The circle cutout has the angle Θ.

Inserting Equation 3.13 into 3.10 gives us the formula for our strain-field

$$\widetilde{e} = \frac{\frac{h}{2}}{R} \quad . \tag{3.14}$$

Applying a voltage extends our PEA, bending our sample further. This leads to a decrease in radius and in turn increase in the displacement of the chip as well as the strain and the corresponding field.

$$\Delta\widetilde{e} = \frac{\delta\widetilde{e}}{\delta R}\Delta R = -\frac{\frac{h}{2}}{R^2}\Delta R \tag{3.15}$$

We already explained that the maximum displacement of the piezo stack is $d_{\text{max}} = 1.2\,\mu\text{m}$ and now assume that our PEA displaces linearly with the applied Voltage. While we do not believe this is the case entirely, our measurements have shown that this assumption is sufficient for our framework. This gives us the change in deflection

$$\Delta z = aU_{\text{b}} \tag{3.16}$$

with the gradient $a = 1.6 \cdot 10^{-8}\frac{m}{V}$ and U_{b} the applied bias voltage. Since we increase our Voltage linearly with the frequency f_b we can rewrite Equation 3.16 to

$$\Delta z = aU_{\text{b}_{\text{total}}} f_{\text{b}} t \tag{3.17}$$

with $U_{\text{b}_{\text{total}}} = 20\,\text{V}$ the total change in voltage. Inserting Equation 3.3 and 3.8 into 3.6 gives us

$$\Delta\widetilde{e}(t) = \frac{\frac{h}{2}\Delta z}{R \cdot z} = \frac{\frac{h}{2} aU_{\text{b}_{\text{total}}} f_{\text{b}} t}{R \cdot z} \quad . \tag{3.18}$$

This allows us to split up our strain field into a constant preload $\widetilde{e}_o$ and a time dependent part

$$\widetilde{e} = \widetilde{e}_o + \Delta\widetilde{e}(t) \quad . \tag{3.19}$$

Differentiating $\widetilde{e}$ gives us the acoustic bias rate, the rate at which our strain-field changes over time,

$$\dot{\widetilde{e}} = \frac{d}{dt}(\widetilde{e}_0 + \Delta\widetilde{e}) = \Delta\dot{\widetilde{e}} = \frac{\frac{h}{2}\Delta z}{R \cdot z} = \frac{\frac{h}{2} a U_{\mathrm{b_{total}}} f_{\mathrm{b}}}{R \cdot z} \tag{3.20}$$

which we can now use to describe our measurements in the framework based on Landau-Zener transitions, introduced in Section 2.4, originally developed for the description of electrically biased resonators. This grants us the ability to express our findings with the dimensionless bias rate

$$\xi = \frac{2\nu_o}{\pi\Omega_{\mathrm{R},0}} = \frac{2\hbar^2\nu_o}{\pi p^2 F_{\mathrm{ac}}^2} \quad . \tag{3.21}$$

We can insert $\nu_0 = 2\frac{\gamma\dot{\widetilde{e}}}{\hbar}$ combined with Equation 3.20 into this framework resulting in

$$\xi = \frac{2\hbar 2\gamma\dot{\widetilde{e}}}{\pi p^2 F_{\mathrm{ac}}^2} = \frac{2\hbar\gamma h U_{\mathrm{b_{total}}} a f_b}{\pi p^2 F_{\mathrm{ac}}^2 R z} \quad . \tag{3.22}$$

3.6.1 Measurement Protocol for Bias Ramps

In the previous section we introduced the bias rate with a linear increase in voltage of the electric field acting upon the PEA. One way to achieve this is to use a triangle signal that continuously changes the asymmetry energy and modifies the loss. This method has the disadvantage that the time between resonant crossings of our tunneling systems can be too short for them to relax back into the ground state, resulting in resonant emissions. This leads to a reduction in loss for higher rates, was can be seen in [Bli22]. Another problem is that the continuously changing signal heats up the sample, which is especially prominent for acoustic biasing, which was observed by [Roz23].

To counteract this, we used an alternative protocol, where the bias voltage changed positively over an interval $t = \frac{1}{2f}$, then remained at 20 V for 6 times that interval and then drops to zero volt with the same interval. This should allow tunneling systems to relax back into their equilibrium state before being swept through the resonance once again. During this time the VNA, supplying the rf-signal that probes our sample, is set to CW time-sweep mode. In this mode, the VNA is set to a single frequency and continuously measures the amplitude S_{21} for a fixed time interval. After the protocol is finished, the driving frequency changes and the process gets repeated.

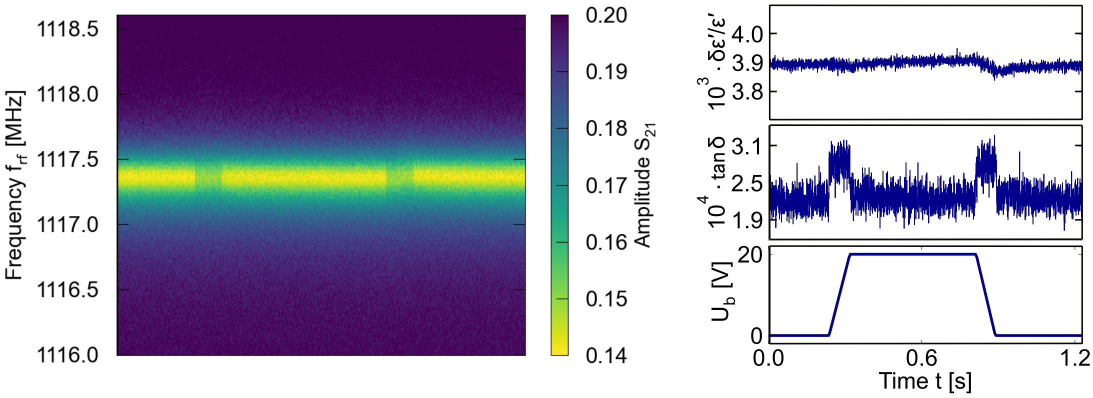

Figure 3.7: On the left is an example of a mapping during an acoustic bias rate measurement. The probe tone power was -99 dBm the interval length was 0.0734 s and the temperature was 30 mK. To increase the clarity, the mapping only shows the first 1.2 s of the protocol, which took around 2.6 s. The mapping depicts the amplitude S_{21} of the rf-signal depending on the time and frequency of the driving field. On the right is the time dependence of the dielectric function extracted from the mapping depicted in Figure 3.6. While the loss increases during changes in $U_\mathbf{b}$ the real part is nearly unaffected.

The VNA measures 12.000 points for every frequency and the time of a single protocol is depended on the if-bandwidth and is around two seconds for our measurements.
An example of the resulting mapping is depicted on the left in Figure 3.7, where the interval was about 0.075 seconds. The resonance frequency of the chip can clearly be identified when the mapping turns yellow, since the amplitude decreases. The time frame where $\dot{U}_\mathrm{b} > 0$ can be easily identified, since the amplitude decreases and the resonance curve broadens during the change.
Now we can take a vertical slices out of the mapping to get a resonance curve for different times during the protocol. With the resonance curve, we can calculate the real part and the loss of the dielectric function, which we explained in Section 3.5.
An example of this process can be seen on the right in Figure 3.7, where we can observe the increased loss during the positive and negative changes in U_b, while the real part remains largely unaffected.

4. Experimental Results

In this chapter, we display the experimental results of this thesis. We start by showing the dielectric response for different probe tone powers and temperatures. In Section 4.2 we focus on the non-equilibrium measurements, where we start off by showing the dielectric response during single ramp acoustic biasing and the difference between increasing and decreasing the strain field voltage during a ramp. We then investigate if the response changes if a preload is applied. The last step is to compare the results during a ramp for different probe tone powers and then plot the loss over the dimensionless bias rate.

4.1 Power and Temperature Dependence

The power and temperature dependence measurements were performed by [Sta25]. Starting with the power dependence, the measurements were performed at a constant temperature of $T = 30\,\mathrm{mK}$. The adjustable attenuator was used to change the probe tone power in the range from -136 dBm to -70 dBm. No strain field was applied during these measurements.

These measurements are important in exploring changes in the dielectric function and saturation effects at different driving-field strengths and are useful in comparison to the steady-state loss at low bias rates shown at a later point.

The results can be seen in Figure 4.1 with the real part on the left and the dielectric loss on the right. The error bars for each point are statistical in nature and represent the standard deviation. The real part is independent of the probe tone power and remains constant. This occurs because all two-level systems influence the real part and the impact of resonant tunneling systems is negligible. With this in mind, changes in the loss can only be attributed to changes in the imaginary part. At low probe tone power, our loss remains constant until a critical point is reached and the loss starts to decrease. After that point, the population difference starts to decrease with higher probe tone powers until saturation sets in and both the loss and population difference approach zero. The measurements validate our theoretical framework and follow the curve shown in Figure 2.3.

The error for both the real part and loss is high at low probe tone power, because the signal-to-noise ratio is small and our data gets distorted.

Following this, we explore the reaction of our sample to different behaviors, in order to confirm that our resonator thermalizes well to the mixing chamber and to explain the measurements. The measurements were performed at a constant probe tone

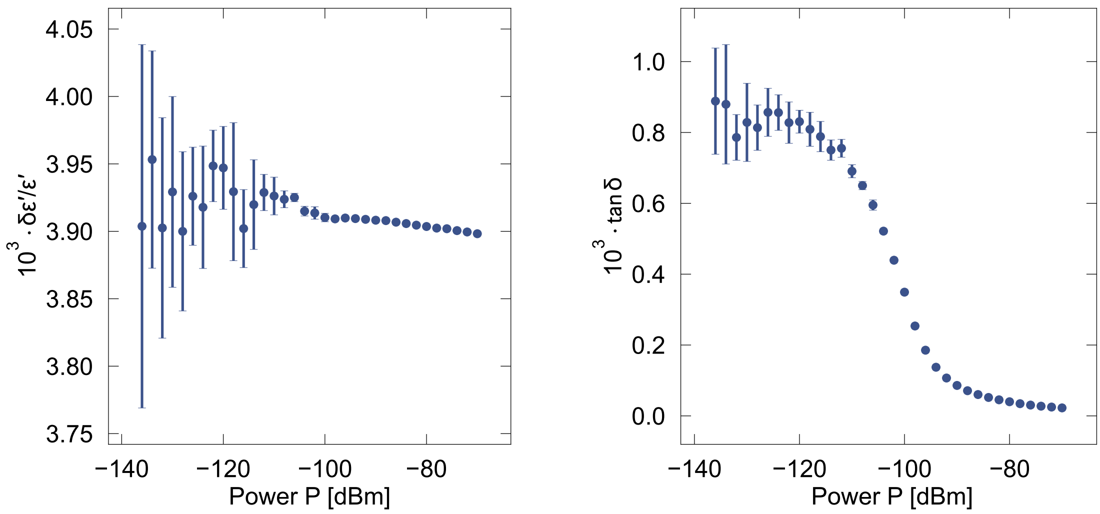

Figure 4.1: Power dependence for the real part and the loss of BS 3.3 at probe tone powers from -136 dBm to -70 dBm and a temperature of T = 30 mK. The real part shows no dependence, while the loss decreases with higher power. Data from [Sta25].

power of -126 dBm, because at this power the loss retains its maximum, while having a passable signal-to-noise ratio. The measurements were performed at temperatures from 7 mK to 5 K. We used $f_{0,\mathrm{ref}} = 1.19\,\mathrm{GHz}$ as the reference frequency, in order to calculate the real part.

The results are shown in Figure 4.2 and we can see that it follows the expected behavior proposed in Section 2.3.6. The real part, seen on the left, is high at lowest temperatures with a small maximum at around 20 to 30 mK. At higher temperatures, the real part decreases because more tunneling systems become thermally saturated. We have a minimum at 3 K after which relaxation behavior becomes important as the relaxation time decreases since it is directly linked to the number of thermal phonons available.

The loss seen on the right also follows the predicted behavior with a plateau at low temperatures, where resonant tunneling systems are all able to fully contribute. This changes at a temperature of around 20 mK where systems with energy splitting near resonance start to become thermally saturated, leading to a steeper slope than in the real part, since only tunneling systems near resonance contribute to the imaginary part. At around 2 K the loss starts to rise again as relaxation processes become the main contributor, which is earlier than in the real part and thus also follows expectation. For high temperatures, our measurements start to deviate from the theory because no plateau can be observed. This is due to the fact that equilibrium measurements at a stable temperature become impossible and our measurement results become unreliable.

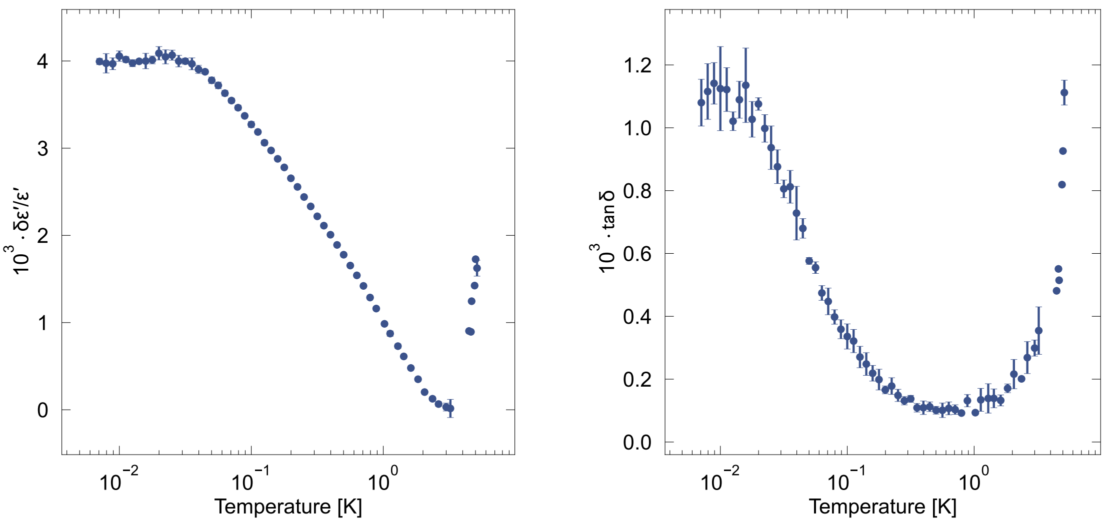

Figure 4.2: Temperature dependence for the real part and the loss of BS 3.3 at a temperature range from $T = 7\,\mathrm{mK}$ to $T = 5\,\mathrm{K}$ and an probe tone power of -126 dBm. The real part and the loss show similar behavior with a maximum at low temperatures that decreases as it gets higher. Data from [Sta25].

4.2 Non-equilibrium Measurements

In this section, we discuss the behavior of amorphous solids under the influence of an additional strain field. We start by exploring how our sample reacts to changes in the strain field and the difference between increasing and decreasing the voltage. We follow this up by increasing the preload acting upon our sample. The next point is to look at the different probe tone powers ranging from -97 dBm to -104 dBm. We end this section by deliberating if the Landau-Zener framework is applicable to acoustic biasing. All measurements were performed at a consistent temperature of $T = 30\,\mathrm{mK}$.

4.2.1 Single Ramp Acoustic Biasing

The first measurements we want to look at were performed at a probe tone power of -99 dBm and can be seen in Figure 4.3 with the real part on the left and the loss on the right. We changed the length of the PEA with the application of an electric bias field. At the start, the bias-field voltage is set to zero and starts to increase to $U_{\mathrm{b_{total}}} = 20\,\mathrm{V}$ over a time-period $1/2f$, resulting in a total increase in length of $0.32\,\mu\mathrm{m}$. Then the voltage remains constant for six times that period and after that decreases to 0 V with the same frequency.
It is plotted in dependence of the acoustic bias rate $\dot{\tilde{e}}$ ranging from $0,85 \cdot 10^{-6}\,\mathrm{Hz}$

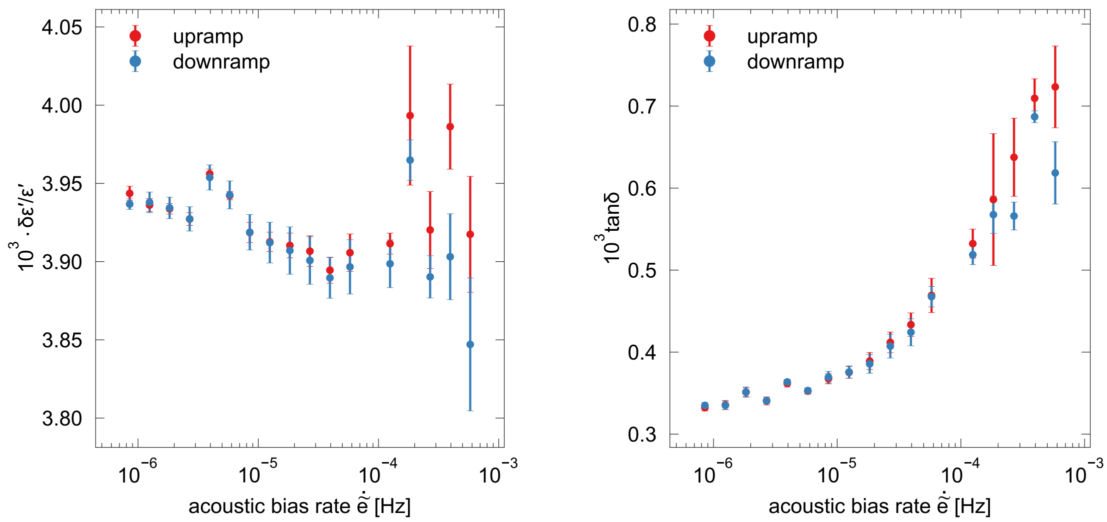

Figure 4.3: Real part (left) and loss (right) of BS 3.3 during a single ramp bias sweep of $U_\mathrm{b} = 20\,\mathrm{V}$. The increase from zero to twenty volt is plotted in red and from twenty to zero in blue. It is plotted for different acoustic bias rates $\dot{\tilde{e}}$. The probe tone power remains constant at -99 dBm.

to $0,58 \cdot 10^{-3}\,\mathrm{Hz}$. The bias rate increases as the time period of a ramp decreases. The real part and the loss during the up-ramp are shown in red, and during the down-ramp in blue.

The real part only has slight changes and can be assumed to be constant, which is expected. As discussed in Section 2.4, the distribution of tunneling system parameters does not change with an applied strain field. Since the distribution stays the same and the influence of resonant tunneling systems is negligible (see Section 4.1), the results validate our assumptions. Heating effects could have an impact on the real part, but have not been observed in our measurements. The difference between the positive and negative change in $\dot{U}_\mathrm{b}$ is small as well, with the result that changes in loss can be attributed to changes in the imaginary part due to resonant behavior. For low and medium bias rates, the loss of positive and negative changes in $\dot{U}_\mathrm{b}$ are similar. This can be explained with the uniform distribution of the tunneling system parameters, leading to an equal number of tunneling systems that increase or decrease their energy splitting. The only relevant factor is thus the rate of change, not the direction. This changes as the bias rate and thus loss increases, and we can observe that the loss during a positive change in $\dot{U}_\mathrm{b}$ tends to be noticeably higher. We assume this is because, for high bias rates, the PEA does not follow the electric field instantly during the negative change in voltage due to its inertia. This phenomenon was also discovered by [Adh21], which they called the hysteresis of the PEA. They also observed a high variance in hysteresis. The error bars are also larger at high rates, since the number of points measured per ramp decreases and the variance in-

creases. The variance increases because the resonance curves become more shallow, resulting in a smaller signal-to-noise ratio. We also had to increase the intermediate frequency bandwidth with higher frequencies, because otherwise there would not be enough points per ramp, to achieve reasonable a resonance resonance curve for fitting.
The shape of the loss curve follows our expectations well. Slow bias rates change the energy splitting of two-level systems within our sample slow enough, so that it can relax back to the ground state and get excited again during a single crossing. The loss at the lowest rates matches the equilibrium loss for -99 dBm shown in Figure 4.1 and also parallels the steady-state limit introduced at the end of Section 2.4. As the rate increases, so does the number of systems that cross the resonance frequency within a small time frame, resulting in an increase in loss. The plateau for high bias rates predicted in Section 2.4 could not be observed, as we were unable to increase the bias rate enough to reach this point. Due to the limitations, set by the instruments, we were limited to the slow bias rates. At this stage, there were only a few points during each ramp with a high variance and because our setup limits us to only increase the voltage by 20 V during a single ramp, we could not increase the number of points.

From this point on only measurements during the positive change in $\dot{U}_\mathrm{b}$ are shown and discussed, as the sample reacts to both ramp directions and we do not have to worry about the possible interference at high bias rates during the negative $\dot{U}_\mathrm{b}$.

4.2.2 Measurements with Increased Preload

The measurements were repeated with the same parameters. The probe tone power was set to -99 dBm, the voltage U_b at 20 V and the bias rate again varied in the range from $0,85 \cdot 10^{-6}$ Hz to $0,58 \cdot 10^{-3}$ Hz. The temperature remained constant at $T = 30$ mK. The only change was an increase in the preload, resulting in an extension in length of the PEA of approximately 0.72 μm. This was achieved by an expansion in the voltage of 45 V, increasing the strength of the electric field acting on our stack and with it it‘s length, so that the voltage oscillates between 45 V and 65 V during the ramps. The comparison of this measurement with the previous one can be seen in Figure 4.4, with the real part on the left and the loss on the right. The measurement with the additional preload is depicted in red, the one without in blue. We can see that the real part remains constant and differences between the measurements are small. We can apply the same explanation as in the previous section, since the preload does not change the arguments made and we also observe that no heating effects take place due to the application of it.
The calculated loss is similar for the measurement with and without preload.
The only noticeable difference is at an acoustic bias rate of $4 \cdot 10^{-3}$ 1/s, where the

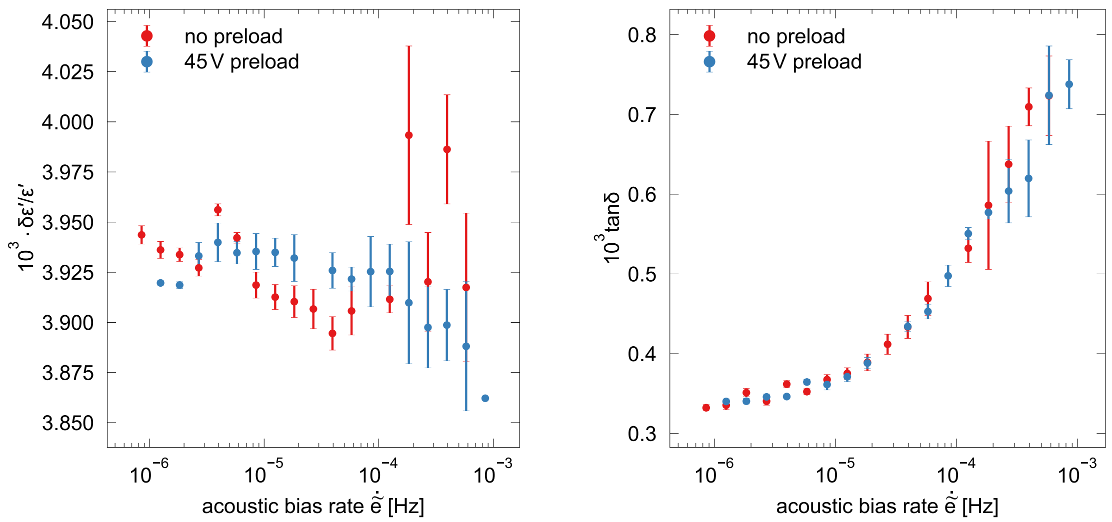

Figure 4.4: Real part (left) and loss (right) of BS 3.3 during a single ramp bias sweep of $U_{\mathrm{b_{total}}} = 20\,\mathrm{V}$. The measurement with no preload is plotted in red and the one with a preload of 45 V in blue. It is plotted for different acoustic bias rates $\dot{\tilde{e}}$. The probe tone power remains constant at -99 dBm.

loss with preload is slightly lower. However, because of the high errors, the points remain within the 3σ range and are statistically within reason. The fact that there is no considerable difference in loss is supported by our framework. The only change in the bias rate is the factor $R \cdot z$, which is negligible at changes this small (see A.1). The similarity also supports the assumption made in Section 3.6, that the length of the PEA and thus the displacement of our sample increases linearly with the applied voltage and validates the equation for the acoustic bias rate. This observation is also consistent with the theory presented in Section 2.3.5. The asymmetry energy Δ is uniformly distributed, with the result that the loss is unaffected by a constant shift in Δ.

4.2.3 Measurements with different probe tone powers

We have determined that the real part and the loss follow the expected behavior during the acoustic bias ramp and that an applied preload has no major effect on the results. We now want to compare the changes in the dielectric function during a single sweep at different probe tone powers.
For that, two additional measurements were made at probe tone powers of $P = -97\,\mathrm{dBm}$ and $P = -104\,\mathrm{dBm}$. The change in voltage during a ramp remained 0-20 V and the acoustic bias rate was varied from $0,85 \cdot 10^{-6}$ Hz to $0,85 \cdot 10^{-3}$ Hz. The temperature during the measurements was $T = 30\,\mathrm{mK}$. The results are shown in

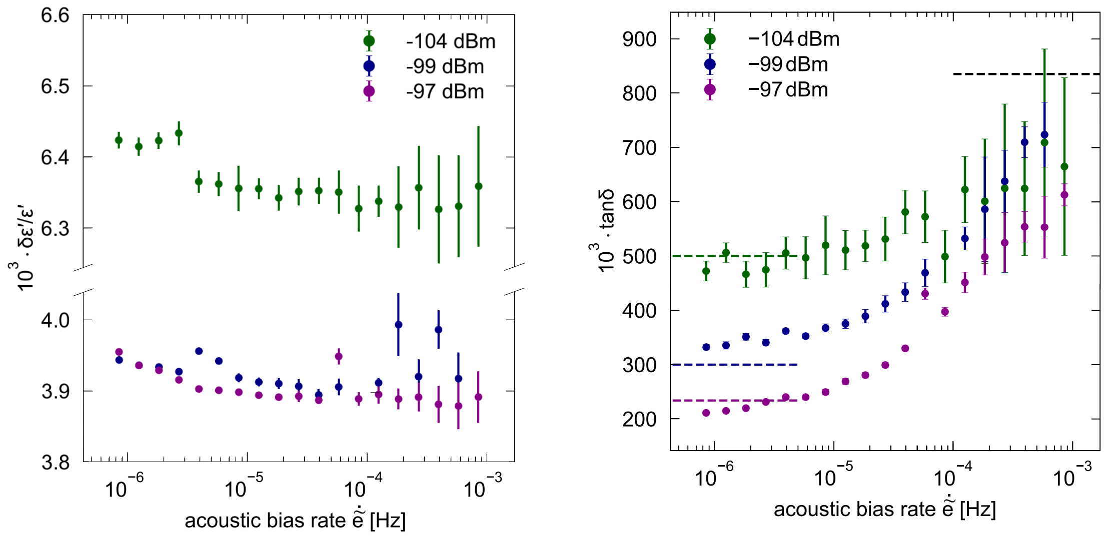

Figure 4.5: real part (left) and loss (right) of BS 3.3 during a single ramp bias sweep of $U_{\mathrm{b_{total}}} = 20\,\mathrm{V}$. The increase from zero to twenty volt is plotted in red, and from twenty to zero is plotted in blue. It is plotted for different acoustic bias rate $\dot{\tilde{e}}$, which are adjusted with frequencies ranging from 0.316 Hz to 215.44 Hz. The probe tone power remains constant at -99 dBm.

Figure 4.5 with the real part on the left and the loss on the right. Starting with the real part, we can see that the constant nature remains the same, while both the error and the total value for the -104 dBm measurement are larger in comparison to the other two. The increased error can be explained with a reduced signal-to-noise ratio at low probe tone powers and follows the results shown in Figure 4.1. Concerning the latter, the total value is directly related to the resonance frequency of the resonator (See Equation 3.7). Before the -104 dBm measurement was conducted, we had to heat the cryostat to room temperature and cool it down again to 30 mK.
This process can slightly change the properties of the resonator, resulting in a small shift in resonance frequency. The change in resonance frequency should not have a major impact on the loss. Turning to the loss, we can observe that at low bias rates the loss approaches the steady-state limit marked by the colored dashed lines for all probe tone powers. We can see that the loss increases at larger bias rates, but we have to note that the results for the measurements at a probe tone power of -104 dBm become unreliable because of the relatively large error, stemming from the bad signal-to-noise ratio. This may also be the reason why the loss for the measurement with a probe tone power of -99 dBm is larger at high bias rates than the one with -104 dBm, which falls outside our expectations. The low power limit, in equilibrium state, taken from the power dependence in Figure 4.1, is marked by the black dotted line and could not be reached, regardless of the probe tone power.

4.2.4 Dimensionless Bias Rate

For the last part, we want to describe our measurements with the dimensionless bias rate ξ introduced in Section 3.6. As a reminder, the dimensionless bias rate is given by

$$\xi = \frac{2\hbar 2\gamma\dot{\tilde{e}}}{\pi p^2 F_{\mathrm{ac}}^2} = \frac{2\hbar\gamma h U_{\mathrm{b_{total}}} a f_b}{\pi p^2 F_{\mathrm{ac}}^2 R z} . \tag{4.1}$$

The driving field strength for the used resonator is calculated with

$$F_{\mathrm{ac}} = \sqrt{\frac{Q^2 P}{Q_{\mathrm{c}} C d^2 \omega_o}} \quad , \tag{4.2}$$

with ω_0 the excitation frequency and the spacing between IDC fingers $d = 2\,\mu$m. The capacitance of our resonator C and the dipole moment d were determined by [Sta25] to be $C = 3.02\,$pF and $P = 1.1\,$D. The deformation potential γ was the only unknown factor, which we determined by fitting our measurements to the mathematically expected loss curve, obtained by numerical integration of Equation 2.72. This can be seen in Figure 4.6, where we used the maximum loss $\tan\delta_0 = 0.835 \cdot 10^{-3}$ to normalize our results and allow for comparison. We determined that a deformation potential of

$$\gamma = 3\,eV \tag{4.3}$$

gives us the best fit between of our data to the mathematical framework. This follows the estimation performed by [Hun76], who found that a deformation potential in the order of 1 eV is necessary to explain the acoustic properties.

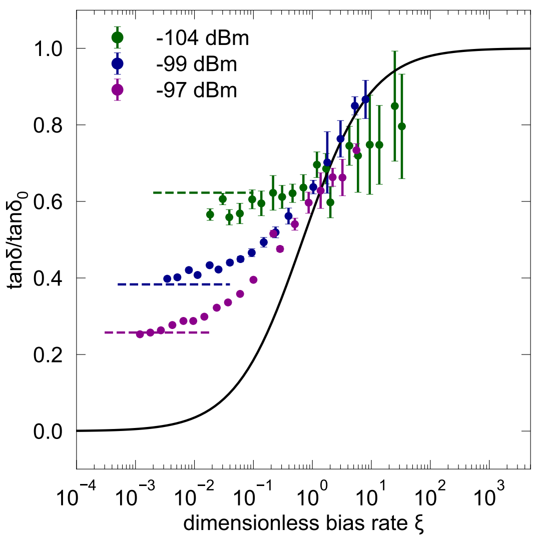

Figure 4.6: Loss plotted against the dimensionless bias rate ξ for different probe tone powers. The back curve shows the numerical solution of Equation 2.72, describing our mathematical framework. The colored dotted lines represent the steady state limit for each probe tone power. The loss is normalized with the maximum loss of $\tan\delta_0 = 0.835 \cdot 10^{-3}$.

We can observe that the introduction of the dimensionless bias rate shifts our curves to the right the more we lower the probe tone power. As the bias rate increases, all curves converge to the expected loss curve shown in black. The data of the measurement with a probe tone power of -104 dBm greatly deviates from the expected loss curve, which can be explained with the same reasoning mentioned in the previous section. The -97 dBm and -99 dBm measurements follow the loss curve closely and deviations are within reason. We can see that the Landau-Zener framework used for describing the effect of electrical bias fields on the dynamics of tunneling system, also works well for acoustic biasing within the used measurement parameters. However, to be sure that the framework fully describes the behavior of glass during acoustic biasing, more measurements in the range of higher bias rates need to be conducted.

5. Summary and Outlook

The goal of this thesis was to examine the dielectric response of borosilicate glass BS 3.3 while slowly increasing an acoustic strain field in a single sweep. We measured the dielectric response by probing the sample with a microfabricated superconducting LC-resonator with a resonance frequency of 1.16 GHz and fitting the resulting rf-signal. The measurements were performed at a constant temperature of 30 mK, which was achieved by placing our sample inside a ^{3}He/^{4}He cryostat. The acoustic bias field was generated with a piezoelectric actuator that bends the sample, inducing a strain field and changing the energy splitting.

We started our discussion by analyzing the equilibrium measurements performed by [Stä25], without an applied strain field, in order to compare and better understand our later results. Both followed the expected behavior, predicted by the standard tunneling model. Concerning the power dependence, the plateau in the loss for low input powers could be observed, as well as the decline for higher input powers. The temperature dependence measurements also followed the expected behavior, decreasing with higher temperatures, while increasing again at around 1 K.
The focus of our experiments were the non-equilibrium measurements. For that, we bent the sample with the piezoelectric actuator that takes advantage of the inverse piezoelectric effect. The actuator changes its length while inside an electric field. In all experiments, we changed the voltage of this electric field by 20 V at different frequencies, resulting in a length change of around 0.32 μm. For all measurements, we observed that the acoustic field had no sizable effect on the real part.
At first we compared the loss for different bias rates and if it made a difference if the actuator extends or contracts. The loss started at the steady state limit for low bias rates and increases with larger bias rates. This follows expectations because at first we sweep slow enough, that tunneling systems can interact resonantly multiple times in a single sweep, while for higher rates more systems are swept through resonance. The expected plateau for high rates was not observed, due to our setup limiting how fast and to what maximum voltage we could ramp the bias. We also observed no difference between increasing or decreasing the length of the actuator for most rates, while at highest rates the time between positive and negative changes in bias voltage was too short, resulting in less loss during the negative change.
We followed this up by exploring if an applied preload, achieved by extending the actuator by 0.72 μm, made a difference in the dielectric response of our sample and were able to confirm that this was not the case. This can be explained by changes in the bias rate due to the preload are negligible and because the tunneling system

parameters are universally distributed the neutral state was not affected.
We then performed the bias sweep without preload for different input powers of -97 dBm, -99 dBm and -104 dBm. While the steady state loss changed according to expectations, the results of the -104 dBm measurement are not meaningful for higher bias rates, because the error is large, stemming from the bad signal-to-noise ratio.
In the last step, we took the Landau-Zener framework developed for electrical biasing and adjusted it for acoustic biasing. We were able to plot our results against the dimensionless bias rate ξ and were able to extract the deformation potential γ by fitting our results to the theoretical loss curve. We found a value of 3 eV to fit the curve best, which agrees with experiments performed by [Hun76], who stated that a deformation potential in the order of 1 eV is necessary to explain acoustic properties.

We can conclude that the energy splitting can be modified with acoustic biasing in a similar way to electrical biasing. We were also able to use the Landau-zener framework to describe our results.
Further experiments could help in understanding the similarities of the different biasing methods. One experiment could explore are measurements with higher bias rates. The signal generator we used to drive the PEA was only able to provide a maximum peak-to-peak voltage of $V_{\mathrm{pp,max}} = 20\,\mathrm{V}$, which limited our range of bias rates, as we had to sweep with high frequencies. As a result, we were unable to reach the fully desaturated state. A different signal generator, which can output higher voltages, should help in providing these measurements.
The interaction between pump fields, fields that change the population difference with the result of mostly excited systems sweeping through resonance, and acoustic bias fields could also help to deepen our understanding of acoustic bias fields.

A. Appendix

A.1 Correlation Between the Deflection and the Change in Radius

As can be seen in Figure 3.6 we imagine the deflection to be circular going through the points $(\pm\frac{D}{2}, 0)$ where the mounting points lie, with $D = 10\,\text{mm}$ and $(0, z)$ the maximum chip deflection. The general equation for circles is given by

$$(x - x_c)^2 + (y - y_c)^2 - R^2 = 0 \tag{A.1}$$

with x_c and y_c beeing the respective coordinates for the center of the circle and x and y the coordinates of a point on the circle. x_c is set to be zero due to the setup. Inserting the three known points results in the equations

$$\left(\frac{D}{2}\right)^2 + y_c^2 - R^2 = 0 \tag{A.2}$$

$$\left(-\frac{D}{2}\right)^2 + y_c^2 - R^2 = 0 \tag{A.3}$$

$$(z - y_c)^2 - R^2 = 0 \quad . \tag{A.4}$$

Solving these equations for y_c results in

$$y_c = \frac{4z^2 - D^2}{8z} \tag{A.5}$$

and the Radius

$$R = \frac{z}{2} + \frac{D^2}{8z} \quad . \tag{A.6}$$

Multiplying Equation A.6 by z gives us

$$Rz = \frac{z^2}{2} + \frac{D^2}{8} \quad . \tag{A.7}$$

The sample can only be deflected to a maximum of $z_{\text{max}} = 300 \cdot 10^{-6}\dot{\text{m}}$ and we can see that $\frac{z_{\text{max}}^2}{2} \ll \frac{D^2}{8} = 12.5\,\mu\text{m}$ and we can thus assume Rz to be constant and unaffected by small changes. With this in mind it can be written as

$$(R + \Delta R) \cdot (z + \Delta z) \approx Rz \quad . \tag{A.8}$$

Solving the equation leads us to

$$\frac{\Delta R}{R} + \frac{\Delta z}{z} + \frac{\Delta R \Delta z}{R z} = 0 \quad . \tag{A.9}$$

The ladder part is negligible for small z giving us the relation

$$\frac{\Delta R}{R} = -\frac{\Delta z}{z} \quad . \tag{A.10}$$

Bibliography

[Adh21] R. Adhikari, K. Doesinger, P. Lindner, B. Faina, and A. Bonanni, *Low temperature and high magnetic field performance of a commercial piezo-actuator probed via laser interferometry*, *Review of Scientific Instruments*, 2021.

[And72] P. W. Anderson, B. I. Halperin, and C. M. Varma, *Anomalous Low-temperature Thermal Properties of Glasses and Spin Glasses*, *Phil. Mag.*, **25**, 1, 1972.

[Bli22] J. Blickberndt, *The Influence of Continuous Electric Bias Fields on the Dielectric Loss of Atomic Tunneling Systems*, Diplomarbeit, Heidelberg University, 2022.

[Bur14] A. L. Burin, A. O. Maksymov, and K. D. Osborn, *Quantum coherent manipulation of two-level systems in superconducting circuits*, *Supercond. Sci. Tech.*, **27**(8), 084001, 2014.

[Car94] H. M. Carruzzo, E. R. Grannan, and C. C. Yu, *Nonequilibrium dielectric behavior in glasses at low temperatures: Evidence for interacting defects*, *Phys. Rev. B*, **50**, 6685–6695, 1994.

[Cla94] J. Classen, C. Enss, C. Bechinger, G. Weiss, and S. Hunklinger, *Low frequency acoustic and dielectric measurements on glasses*, *Ann. Physik*, **3**, 315, 1994.

[Cla00] J. Classen, T. Burkert, C. Enss, and S. Hunklinger, *Anomalous Frequency Dependence of the Internal Friction of Vitreous Silica*, *Phys. Rev. Lett.*, **84**, 2176–2179, 2000.

[Deb12] P. Debye, *Zur Theorie der spezifischen Wärmen*, *Ann. Physik*, **344**, 789, 1912.

[Deb13] P. Debye, *On the theory of anomalous dispersion in the region of long-wave electromagnetic radiation*, *Verh. Deut. Phys. Gesell.*, **15**, 777–793, 1913.

[Dou80] P. Doussineau, C. Frénois, R. G. Leisure, A. Levelut, and J.-Y. Prieur, *Amorphous-like acoustical properties of Na doped* $\beta - Al_2O_3$, *J. Phys France*, **41**, 1193, 1980.

[Ens89] C. Enss, C. Bechinger, and M. Von Schickfus, *Phonons 89*, 474, World Scientific, Singapur, 1989.

[Ens05] C. Enss and S. Hunklinger, *Low-Temperature Physics*, Springer, Heidelberg, 2005.

[Fre16] B. Frey, *Entwicklung mikrostrukturierter supraleitender Resonatoren zur breitbandigen Untersuchung dielektrischer Eigenschaften zwischen 37 MHz und 1GHz bei tiefen Temperaturen*, Master's thesis, Heidelberg University, 2016.

[Fre21] B. Frey, *Landau-Zener spectroscopy of bulk glasses*, Dissertation, Heidelberg University, 2021.

[Fro77] G. Frossati, J. le G. Gilchrist, J. C. Lasjaunias, and W. Meyer, *Spectrum of low-energy dipolar states in hydrated vitreous silica*, *J. Phys. C*, **10**(18), L515–L519, 1977.

[Hun72] S. Hunklinger, W. Arnold, S. Stein, R. Nava, and K. Dransfeld, *Saturation of the ultrasonic absorption in vitreous silica at low temperatures*, *Phys. Lett. A*, **42**(3), 253–255, 1972.

[Hun74] S. Hunklinger, *Ultrasonics in Amorphous Materials*, *Proc. Ultrasonic Symp. (IEEE)*, 1974.

[Hun76] S. Hunklinger and W. Arnold, 3 - ultrasonic properties of glasses at low temperatures, Volumen 12 in *Phys. Acoust.*, 155 – 215, Academic Press, 1976.

[Hun77] S. Hunklinger, Acoustic and dielectric properties of glasses at low temperatures, in J. Treusch (Ed.), *Festkörperprobleme 17*, Volumen 17 in *Advances in Solid State Physics*, 1–11, Springer Berlin Heidelberg, 1977.

[Jä72] J. Jäckle, *On the ultrasonic attenuation in glasses at low temperatures*, *Z. Phys. A*, **257**(3), 212, 1972.

[Ku05] L. C. Ku and C.C. Yu, *Decoherance of a joseph qubit due to coupling to two-level-systems*, *Phys. Rev. B.*, **72**, 163601, 2005.

[Lan32] L.D. Landau, *On the Theory of Transfer of Energy at Collisions II*, *Phys. Z. Sowjetunion*, **2**(46), 118, 1932.

[Lis15] J. Lisenfeld, G. J. Grabovskij, C. Müller, J. H. Cole, G. Weiss, and A. V. Ustinov, *Observation of directly interacting coherent two-level systems in an amorphous material*, *Nature Communications*, **6**, 2015.

[Luc16] A. Luck, *Nuclear spin dominated relaxation of atomic tunneling systems in glasses*, Dissertation, Heidelberg University, 2016.

[Mat63] B. T. Matthias, T. H. Geballe, and V. B. Compton, *Superconductivity*, *Rev. Mod. Phys.*, **35**, 1–22, 1963.

[Phi72] W. A. Phillips, *Tunneling States in Amorphous Solids*, *J. Low Temp. Phys.*, **7**(3/4), 351, 1972.

[Phi81] W. A. Phillips (Ed.), *Amorphous solids*, Volumen 24 in *Topics in current physics*, Springer, Heidelberg, 1981.

[Pro15] S. Probst, F. B. Song, P. A. Bushev, A. V. Ustinov, and M. Weides, *Efficient and robust analysis of complex scattering data under noise in microwave resonators*, *Rev. Sci. Instrum.*, **86**(2), 024706, 2015.

[Rog97] S. Rogge, D. Natelson, B. Tigner, and D. D. Osheroff, *Nonlinear dielectric response of glasses at low temperature*, *Phys. Rev. B*, **55**(17), 11256, 1997.

[Roz23] P. Rozov, *Comparison between the Influence of Acoustic Properties of N-BK7 at Low Temperatures*, Bachelor's thesis, Heidelberg University, 2023.

[Sar16] B. Sarabi, A. N. Ramanayaka, A. L. Burin, F. C. Wellstood, and K. D. Osborn, *Projected Dipole Moments of Individual Two-Level Defects Extracted Using Circuit Quantum Electrodynamics*, *Phys. Rev. Lett.*, **116**, 167002, 2016.

[Sta25] C. Staender, Dissertation, Heidelberg University, 2025.

[Zac32] W. H. Zachariasen, *The Atomic Arrangement In Glass*, *Journal of the American Chemical Society*, **54**(10), 3841–3851, 1932.

[Zel71] R. C. Zeller and R. O. Pohl, *Thermal Conductivity and Specific Heat of Noncrystalline Solids*, *Phys. Rev. B*, **4**(6), 2029, 1971.

[Zen32] C. Zener and R. H. Fowler, *Non-adiabatic crossing of energy levels*, *Proc. R. Soc. London*, **137**(833), 696–702, 1932.

Danksagung

Hiermit möchte ich mich bei den Leuten bedanken, die es mir ermöglicht haben, diese Arbeit zu verfassen. Ich bedanke mich insbesondere bei:

Prof. Dr. Christrian Enss für die Betreuung meiner Arbeit und dem freundlichen aufnehmen in die Arbeitsgruppe,

PD Dr. Loredana Gastaldo für die freundliche übernahme meiner Zweitkorrektur ,

Dr. Andreas Reiser für den tollen Einstieg in die Laborarbeit und das Korrekturlesen meiner Bachelorarbeit,

Christian Ständer für die tolle Betreuung und Zusammenarbeit im Labor, sowie die konstruktieve Diskussion über Messergebnisse und das Korrektturlesen meiner Arbeit

Jan Blickberndt und Lukas Münch für die Bereitschafft mit mir die Theorie durchzugehen und mir beim verständnis zu helfen

Rudolf Eitel für die Versorgung des Experimentes mit flüssigem Helium,

Beatrice Schwöbel für die Hilfe bei der Organisatotion,

Allen weiteren Mitgliedern der Arbeitsgruppen F3 und F4 für die täglichen interessanten Gespräche in der Kaffeeecke

Lukas Storz und Mira Stoll für das Korrekturlesen und Ausbessern der Arbeit.

Ich versichere, dass ich diese Arbeit selbstständig verfasst und keine anderen als die angegebenen Quellen und Hilfsmittel benutzt habe.

Heidelberg, den 13.03.2025

J.Herbrich ....

(Jonathan Herbrich)